electronics

MDPI

Article

Backstepping Based Super-Twisting Sliding Mode MPPT Control with Differential Flatness Oriented Observer Design for Photovoltaic System

Rashid Khan [1], Laiq Khan [2], Shafaat Ullah [1,3], Irfan Sami [4] and Jong-Suk Ro [4,*]

1 Department of Electrical and Computer Engineering, COMSATS University Islamabad, Abbottabad Campus, Abbottabad 22060, Pakistan; rasheedkhan028@gmail.com (R.K.); engr.shafaat@uetpeshawar.edu.pk (S.U.)
2 Department of Electrical and Computer Engineering, COMSATS University Islamabad, Islamabad 45550, Pakistan; laiqkhan@comsats.edu.pk
3 Department of Electrical Engineering, University of Engineering and Technology Peshawar, Bannu Campus, Bannu 28100, Pakistan
4 School of Electrical and Electronics Engineering, Chung-Ang University, Dongjak-gu, Seoul 06974, Korea; irfansamimwt@gmail.com
* Correspondence: jongsukro@gmail.com

Received: 20 August 2020; Accepted: 18 September 2020; Published: 21 September 2020

check for updates

Abstract: The formulation of a maximum power point tracking (MPPT) control strategy plays a vital role in enhancing the inherent low conversion efficiency of a photovoltaic (PV) module. Keeping in view the nonlinear electrical characteristics of the PV module as well as the power electronic interface, in this paper, a hybrid nonlinear sensorless observer based robust backstepping super-twisting sliding mode control (BSTSMC) MPPT strategy is formulated to optimize the electric power extraction from a standalone PV array, connected to a resistive load through a non-inverting DC–DC buck-boost power converter. The reference peak power voltage is generated via the Gaussian process regression (GPR) based probabilistic machine learning approach that is adequately tracked by the proposed MPPT scheme. A generalized super-twisting algorithm (GSTA) based differential flatness approach (DFA) is used to retrieve all the missing system states. The Lyapunov stability theory is used for guaranteeing the stability of the proposed closed-loop MPPT technique. The Matlab/Simulink platform is used for simulation, testing and performance validation of the proposed MPPT strategy under different weather conditions. Its MPPT performance is further compared with the recently proposed benchmark backstepping based MPPT control strategy and the conventional MPPT strategies, namely, sliding mode control (SMC), proportional integral derivative (PID) control and the perturb-and-observe (P&O) algorithm. The proposed technique is found to have a superior tracking performance in terms of offering a fast dynamic response, finite-time convergence, minute chattering, higher tracking accuracy and having more robustness against plant parametric uncertainties, load disturbances and certain time-varying sinusoidal faults occurring in the system.

Keywords: backstepping; buck-boost; DC–DC converter; differential flatness approach (DFA); maximum power point tracking (MPPT); photovoltaic (PV); sliding mode control (SMC); super-twisting algorithm (STA)

1. Introduction

Electrical energy production has been a challenging task throughout history. With the industrialization of countries, the energy demand is growing proportionally. Most of the energy production nowadays comes from depleting fossil fuels causing environmental concerns in terms of greenhouse gas emission, global warming and increased pollution. Furthermore, due to the economic and petroleum crisis nowadays, together with increasing efforts for environmental protection, scientific research has now focused on the development of so-called alternative or renewable energy sources [1,2].

Among different forms of the alternative energy sources, electricity generation from solar energy through photovoltaic (PV) cells is regarded as the fast developing technology due to considerable reduction in its equipment cost. It is a naturally and abundantly available clean energy, distributed all over the earth, and can compete with other sources of energy production [2,3]. Despite all the stated attractive attributes of the PV cells, its energy conversion efficiency is still very low. The PV cell has a nonlinear current-voltage and power-voltage (i.e., $I - V$ and $P - V$, respectively) characteristics that vary considerably with the ambient environmental conditions (i.e., temperature and irradiance). Only, under a uniform solar irradiance, the PV cell exhibits a unique operating point, called the maximum power point (MPP), where the maximum voltage and current (i.e., V_{MPP} and I_{MPP}, respectively) occurs. This makes the maximum power extraction from the PV cell quite a challenging task under inconsistent atmospheric conditions. Hence, to maximize the efficiency and to extract and transfer the maximum possible power from the PV cell to a load, a sophisticated control strategy is needed, known as the maximum power point tracking (MPPT). The MPPT strategy matches the load resistance with the source (PV cell) resistance, thus forcing the PV cell to operate on the MPP and ensuring the maximum power extraction, despite ambient atmospheric variations or the load. The PV system operation in the MPPT mode also, indirectly, reduces the total number of PV cells required and, hence, its total cost. [4–7].

The MPPT algorithm is typically integrated into the power electronic converter serving as a hardware interface between the PV cell (source) and the load. This algorithm continuously alters the duty cycle, d, of the power converter switches and adapts the PV system operating point (MPP or V_{MPP}) to the varying atmospheric conditions, thus ensuring the optimal power extraction from it [8–11].

To maximize the power output of a PV system, conventionally, hill climbing strategies are used. These strategies include a number of variants of the two basic algorithms, such as: Perturb-and-observe (P&O) and incremental conductance (IncCond). Both of these stated strategies try to find the MPP of the PV system by introducing oscillations in the output, even if the MPP is reached. Thus, the overall efficiency of the PV system is reduced. However, the IncCond algorithm causes less oscillations than the P&O. Similarly, under rapidly varying atmospheric conditions, the IncCond algorithm performs better than the P&O technique. However, it needs additional control circuitry for proper operation, thus making its implementation more complex [12].

Owing to the nonlinear nature of the electrical characteristics of the PV cell and power converter, different nonlinear MPPT control strategies have been reported in the available scientific literature. In [13], a conventional backstepping based nonlinear MPPT scheme has been proposed for a standalone PV system. However, a significant steady-state error was observed in the output during MPP tracking. This issue has been addressed in [12] through integral backstepping based nonlinear MPPT algorithm, where the output tracking error was reduced to a minute level due to the integral action. Similarly, another nonlinear robust backstepping based MPPT paradigm has been proposed in [14]. This stated strategy not only dealt efficiently with the simultaneous variation of the temperature and irradiance, but also it offered significant robustness against time-varying sinusoidal faults and parametric uncertainties occurring in the system.

In the context of nonlinear control, the backstepping strategy belongs to the recursive control design. It acquires its name from the recursive nature of the controller design, where the design process starts with an inner scalar equation that steps-back towards the external control input after passing through a chain (or sequence of integrators). Its application is based on designing a nonlinear controller recursively by choosing some of the system state variables as the virtual controllers, followed by designing intermediate control laws for these selected virtual controllers. Its attractive attributes are fast dynamic response, external disturbance rejection, robustness to system parametric uncertainties as well as modeled and unmodeled system dynamics. It has the capability of canceling out all the destabilizing effects (i.e., forces or terms) appearing throughout the domain [15,16].

Another well-established nonlinear MPPT control strategy is the conventional sliding mode control (CSMC). It is a robust control strategy based on the variable-structure control (VSC) theory. The key to CSMC implementation is the reduction of the higher order complex closed-loop system to the first order, namely the sliding variable along with its derivative. Consequently, the plant order is reduced, thus the main control design is focused on the reduced plant dynamics. The main attributes of the CSMC include: Simple implementation, good dynamic response, external disturbance rejection and low sensitivity to (internal) plant parametric uncertainties (or variations). However, the main negative aspect of the first-order CSMC is the high-frequency oscillations in the system states, called the chattering phenomenon, resulting from the switching action of the discontinuous control signal as well as other non-idealities (e.g., hysteresis, time-delays, unmodeled system dynamics etc.) [17–19]. The chattering leads to a low control accuracy, increased heat losses in the power electronic circuits, and high wear and tear in case of moving mechanical parts [20].

To attenuate chattering, several nonlinear higher order sliding mode control (HOSMC) strategies can be found in the available literature, such as the super-twisting algorithm (STA) [21]. The STA is a second-order SMC strategy where the control signal appears in the first derivative of the sliding variable. Moreover, unlike other second-order SMC strategies, it is applicable to a system (of any order, in general). Some of the main features of the STA are given as follows [18,19,22,23]:

1. It offers a finite-time convergence of the output as well its derivative to the origin.
2. It can compensate those perturbations/uncertainties that are Lipschitz
3. It requires the information of the output only (the sliding variable)
4. It introduces an extra integrator (dynamic extension) to the control structure in such a manner that the discontinuous control term is hidden behind this integrator. Thus, it artificially increases the plant relative degree and generates a continuous control signal, thereby attenuating chattering.

Motivation and Significant Contributions

The main motivation of this article is to formulate an MPPT control strategy for a PV system with minute chattering and at the same time offering a high precision performance under different atmospheric conditions and internal as well as external disturbances.

For this purpose, a hybrid sensorless observer based nonlinear robust backstepping super-twisting sliding mode control (BSTSMC) MPPT paradigm is proposed in this article for delivering an optimum power from a PV array to a resistive load through a DC–DC converter. The reference peak power voltage is generated via the Gaussian process regression (GPR) based probabilistic machine learning approach that is adequately tracked by the proposed MPPT scheme. A generalized super-twisting algorithm (GSTA) based differential flatness approach (DFA) is used to observe all the missing system states. The Lyapunov stability theory is used for guaranteeing the stability of the proposed closed-loop MPPT technique. The MPPT performance of the proposed control strategy is simulated, tested, validated and compared with the recently proposed benchmark backstepping [13] based MPPT strategy and conventional SMC, PID and P&O based MPPT techniques, in Matlab/Simulink, under simultaneous variation of the temperature, irradiance and load. It is observed that the proposed BSTSMC based MPPT technique offers a superior tracking performance in terms of offering a fast dynamic response, finite-time convergence, minute chattering, higher tracking accuracy and having more robustness against plant parameters perturbations, load disturbances and certain time-varying sinusoidal faults occurring in the system.

As per the available scientific literature, following are the significant contributions made by this research article:

1. To the best of the authors knowledge, model based backstepping STA, for MPPT control of the PV system, has never been applied before.
2. The authors also claim that the DFA based observer using GSTA has never been implemented for states retrieval before.

3. The GPR based voltage generation trajectory also contributes to the scientific literature.

The entire article is organized as follows: Section 1 covers the introduction and background literature review to this article. Section 2 is dedicated to the PV system modeling. Section 3 discusses the PV array reference peak power voltage generation. Section 4 describes the averaged state-space modeling of the DC–DC converter. Section 5 presents the differential flatness based system states observer design. Section 6 is about the proposed MPPT control scheme design. Section 7 discusses the performance validation of the proposed MPPT scheme in Matlab/Simulink. Finally, Section 8 presents concluding remarks to this article.

2. Phtovoltaic Array Mathematical Modeling

A PV cell generates electricity (DC) from sunlight using the photoelectric effect. For getting an increased voltage and current output, PV cells are connected in series and parallel combination, respectively. Series connection of PV cells forms a PV module or panel, series connection of PV modules constitutes a PV string, while parallel connection of PV strings makes a PV array.

Depending on their complexity and accuracy, a PV cell can be represented by several different equivalent circuit models, including: Single-diode, two-diode and three-diode equivalent circuit model. Taking into account its simplicity and reasonable accuracy, the most commonly used equivalent circuit model is the single-diode model of the PV cell [24], as illustrated in Figure 1. Where, R_s and R_p indicate the PV cell equivalent series and shunt resistances, respectively. Normally, $R_s << R_p$, where R_s exists due to the metallic leads resistances, while R_p due to the leakage current of the PN-junction. Furthermore, I_{ph}, I_D, I_p, I and V are the photon-generated current, diode current, current through the equivalent shunt-resistance, cell output current and cell output voltage, respectively. Mathematically, the PV cell output current can be worked out from Figure 1 by applying Kirchhoff's current law at the junction, as follows:

$$I = I_{ph} - \underbrace{I_0 \left[e^{\frac{q}{AkT}(V+IR_s)} - 1 \right]}_{I_D} - \underbrace{\frac{V+IR_s}{R_p}}_{I_p} \tag{1}$$

In Equation (1), I_D indicates the Shockley diode equation, I_0 represents the diode leakage (or reverse saturation) current, q equals the electron charge (1.6×10^{-19} C), k is the Boltzmann constant (1.38×10^{-23} J/K), T represents the PN-junction temperature (in Kelvin) and A denotes the diode ideality factor (or constant), where usually: $1 \leq A \leq 1.50$.

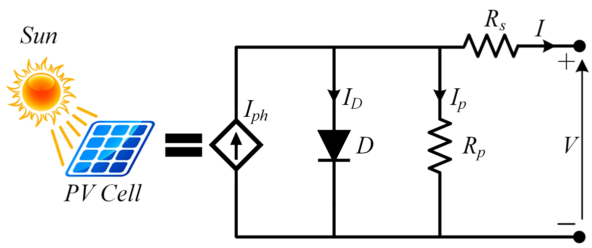

Figure 1. Single-diode equivalent circuit model of a photovoltaic (PV) cell.

For practical applications, many PV cells are connected in series and parallel combination to obtain higher voltage and current output, respectively. Suppose, N_p and N_s be the number of parallel connected PV modules and series connected PV cells, respectively. Then, the mathematical relation between the PV array output current, i_{pv}, and output voltage, v_{pv}, can be expressed as follows [25]:

$$i_{pv} = N_p I_{ph} - N_p I_0 \left[e^{\frac{q}{AkT}\left(\frac{v_{pv}}{N_s} + \frac{i_{pv} R_s}{N_p}\right)} - 1 \right] - \frac{N_p}{R_p} \left(\frac{v_{pv}}{N_s} + \frac{i_{pv} R_s}{N_p} \right) \tag{2}$$

In this work, a user-defined PV array with a total power output of 24.880 W is employed. Overall, it has 16 PV modules, where 4 modules are connected in a series combination in each string, and then 4 strings are connected in a parallel combination to constitute the complete PV array. Table 1 describes various electrical and physical parameters of the PV array, under standard test conditions (STC), i.e., 25 °C and 1000 W/m^2. Moreover, the PV array electrical characteristics ($I - V$ and $P - V$), are‘depicted in Figure 2.

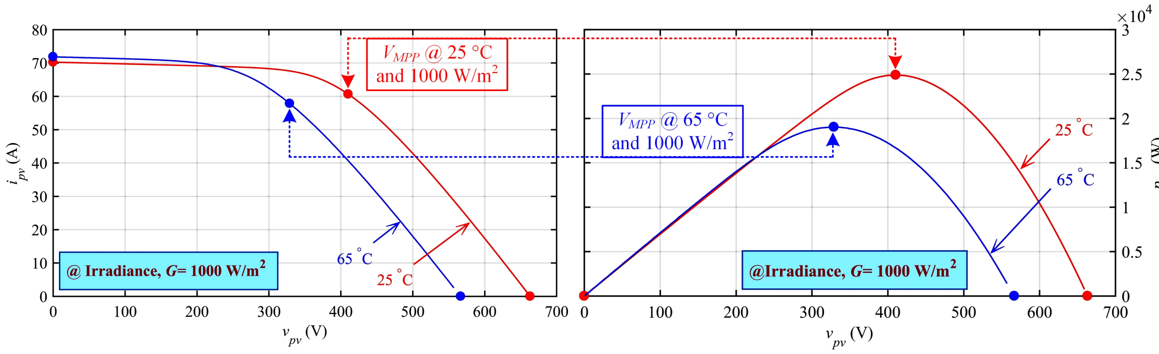

Figure 2. Electrical characteristics of the PV array.

3. Reference Voltage Generation via Gaussian Process Regression

The MPPT controller must continuously track the PV array output voltage, v_{pv}, to its reference, V_{MPP} or v_{pv}^r for delivering the maximum available power to the load. Because, the reference voltage varies with the inconsistent weather conditions, that is, the temperature, (T, °C), and solar irradiance, (G, W/m^2). Different approaches have been used to estimate/learn the PV array reference peak power voltage, such as regression plane [12,13], Takagi-Sugeno-Kang based adaptive NeuroFuzzy Inference System (ANFIS) [14] and Gaussian process regression (GPR) based learning approaches [26]. In this article, a GPR based probabilistic machine learning procedure is employed for V_{MPP} estimation/learning of the PV array.

Definition 1. *A Gaussian process (GP) can be defined as the collection of random variables, where any finite number of those random variables have a joint Gaussian distribution* [27].

The GPs put a prior over functions in order to obtain posterior over functions, for some data being observed. When some random function $f(x)$ follows a GP, it is indicated by a combination of a mean function and a covariance (or kernel) function, as follows:

$$f(\mathbf{x}) \sim \mathcal{GP}\left(\mu(\mathbf{x}), \mathcal{K}\left(\mathbf{x}, \mathbf{x}'\right)\right)$$

where $f(\mathbf{x})$ and $\mathcal{GP}$ indicate a real process and a Gaussian process, respectively, $\mathbf{x}$ and $\mathbf{x}'$ are the arbitrary input variables (normally represented as vectors, because there are many input variables), $\mu(\mathbf{x}) = \mathbb{E}[(\mathbf{x})]$ represents the mean function, $\mathbb{E}[(\mathbf{x})]$ is the expectation of $(\mathbf{x})$ and $\mathcal{K}(\mathbf{x}, \mathbf{x}') = \mathbb{E}\left[(f(\mathbf{x}) - \mu(\mathbf{x}))\left(f\left(\mathbf{x}'\right) - \mu\left(\mathbf{x}'\right)\right)\right]$ describes the covariance (or kernel) function evaluated at $\mathbf{x}$ and $\mathbf{x}'$, which is sometimes also known as the kernel trick.

Definition 2. *A function $\mathcal{K}$, capable of mapping a pair of input arguments $\mathbf{x}$ and $\mathbf{x}'$ into $\mathbb{R}$ (real numbers) is known as a kernel* [27].

The covariance function encodes all of the assumptions about the function to be learnt, thus making it a crucial ingredient in GP predictor. Any function could be selected as a valid covariance function, as long as its resulting covariance matrix remains positive semi-definite. Nonetheless, in some learning processes, the input arguments are not necessarily vectors. For such scalar inputs, the most commonly used kernel function is the squared exponential kernel ($\mathcal{K}_{SE}$). It is expressed as follows:

$$\mathrm{cov}\left(f(\boldsymbol{x}), f\left(\boldsymbol{x}'\right)\right) = \mathcal{K}_{SE}\left(\boldsymbol{x}, \boldsymbol{x}'\right) = \exp\left(-\frac{r^2}{2\ell^2}\right) = \exp\left(-\frac{|\boldsymbol{x}-\boldsymbol{x}'|^2}{2\ell^2}\right) \tag{3}$$

where parameters r and ℓ represent the radial basis function and characteristic length-scale, respectively.

It can be seen in Equation (3) that the covariance between the outputs is expressed as a function of the inputs. It means that the covariance, for this particular covariance function, reaches almost unity between the output variables, if the corresponding inputs are close enough. On the other hand, it decreases if the distance between the inputs increases.

In this article, a GPR based V_{MPP} learning process is carried out in Matlab/Simulink using the Regression Learner App. In this process, GPR learns three different variables at a time, that is, it takes the two atmospheric variables (i.e., temperature and solar irradiance) as two input arguments (i.e., known predictors or data) and then maps these variables to their corresponding V_{MPP} (i.e., known response). A trained GPR model, based on the squared-exponential kernel function, is obtained that renders new predicted responses for any new input data.

For GPR based V_{MPP} learning process, the V_{MPP} data is recorded by entering the user-defined PV array specifications, given in Table 1, in Matlab/Simulink. During this process, the temperature is perturbed from 0 °C to 75 °C in uniform steps of 1 °C. On the other hand, the solar irradiance is perturbed from 1 W/m^2 to 1000 W/m^2, in uniform steps of 1 W/m^2. As a result, about 76,000 V_{MPP} data points are recorded. The concept of GPR based V_{MPP} learning workflow is depicted in Figure 3. Moreover, the predicted response of the trained GPR model against the true (or actual) response is depicted in Figure 4. As, the predicted response closely matches the true response (i.e., the diagonal line), it indicates that the prediction error is very small and the learning process renders a good trained GPR model. This trained GPR model then generates the reference voltage, V_{MPP}, during simulation for any combination of input temperature and irradiance levels that is tracked by the MPPT controller.

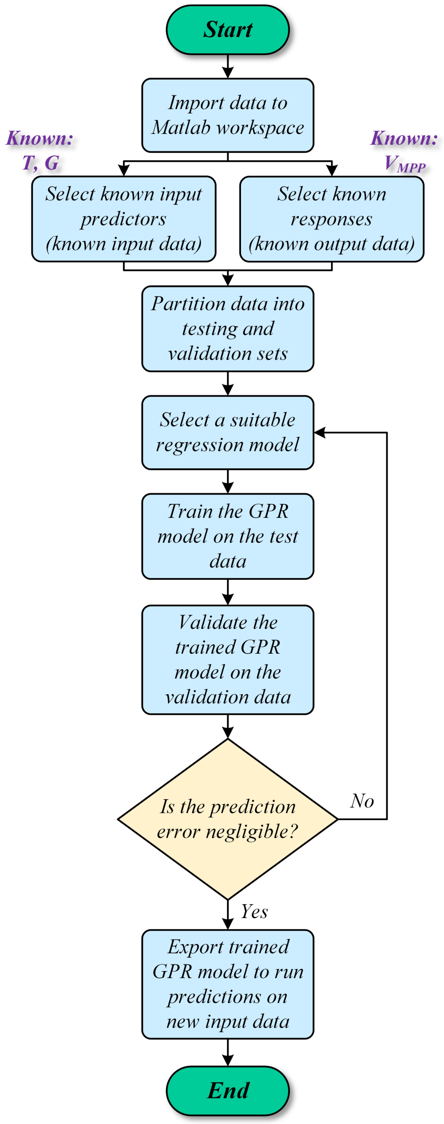

Figure 3. Gaussian process regression (GPR) based V_{MPP} learning workflow.

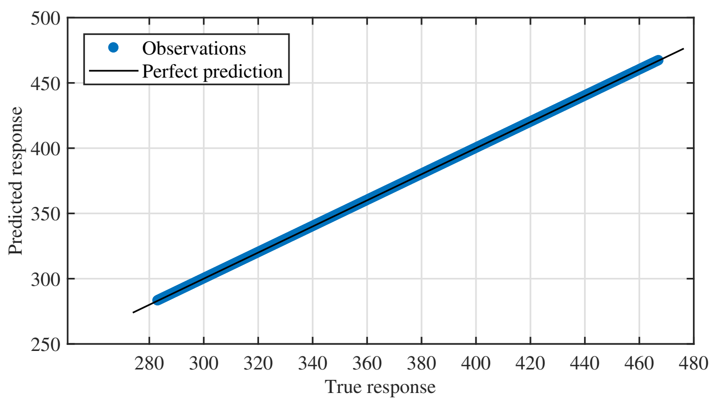

Figure 4. Predicted and true response comparison of the trained GPR model.

4. State-Space Averaged Discrete-Time Bilinear Equivalent Circuit Modeling of the Cascaded Non-Inverting DC-DC Buck-Boost Power Converter

For operating the PV array at its MPP, irrespective of inconsistent atmospheric conditions, the MPPT control algorithm is integrated into the power electronic converter serving as a hardware interface between the PV array (source) and the load. This algorithm constantly adjusts the duty cycle, d, of the power converter switches and adapts the PV array operating point (V_{MPP}) to the varying atmospheric conditions, thus ensuring the optimal power extraction from it [8].

Several well-known versions of the DC–DC power converters have been employed as the hardware interface between the PV array and the load, specifically, conventional buck-boost converter, Cuk converter, and single-ended primary inductor (SEPIC) converter. However, all the stated converter variants are prone to high switching stresses, and consequently lower efficiency. Moreover, the output voltage polarity is reversed with respect to the input voltage polarity (or the output voltage polarity is negative with respect to the common ground), specifically in case of the conventional buck-boost converter and the Cuk converter. These stated issues are resolved by using a cascaded non-inverting DC–DC buck-boost (CCNI-BuBo) converter, which is a cascaded combination of a buck converter and a boost converter. Its output voltage is either less than, or higher than in magnitude than its input voltage. Moreover, the output voltage polarity is the same with respect to the input voltage polarity. It has two controllable switches (S_1 and S_2), an inductor (L) and two capacitors (C_1 and C_2) in its circuit. It can be operated in three separate modes, that is, the buck mode (when S_1: Switching and S_2: OFF), the boost mode (when S_1: ON and S_2: Switching) and the buck-boost mode (when both S_1 and S_2: Simultaneously switching) [28].

Conventionally, the switching power converters have time-variant nonlinear response. So, to give a better physical insight into a converter operation and properties, different equivalent circuit modeling techniques are used. If the accuracy is not a big concern, a converter can be approximately represented by its continuous, time-invariant and linear equivalent circuit model using the small-signal approximation that are easier to analyze. Since, a switching power converter basically behaves as a sampled system, hence, for a higher level of accuracy it must be represented by its state-space averaged discrete-time bilinear equivalent circuit model that includes the product of the duty cycle, d, and system states [29,30].

In this research work, the state-space averaged discrete-time bilinear equivalent circuit modeling technique is employed to develop an equivalent circuit model for the CCNI-BuBo converter serving as power electronic interface between the PV array and the resistive load, R_L, as illustrated in Figure 5. Different significant parameters of the converter are expressed in Table 1. Let the converter operates in the continuous conduction mode (CCM), then, there are two different switching modes of operation for the CCNI-BuBo converter. That is, Mode 1: Both S_1 and S_2 are ON, while both D_1 and D_2 remain OFF. Mode 2: Both S_1 and S_2 remain OFF, while both D_1 and D_2 are ON. That is, the converter is operated in the buck-boost mode. Now, the state-space model for operation in Mode 1 of the stated converter, in compact vector-matrix form, can be expressed as follows:

$$\underbrace{\begin{bmatrix} \dot{v}_{pv} \\ \dot{i}_L \\ \dot{v}_{C_2} \end{bmatrix}}_{\dot{\mathbf{x}}} = \underbrace{\begin{bmatrix} 0 & -\frac{1}{C_1} & 0 \\ \frac{1}{L} & 0 & 0 \\ 0 & 0 & -\frac{1}{R_L C_2} \end{bmatrix}}_{\mathbb{A}_{\mathbf{on}}} \underbrace{\begin{bmatrix} v_{pv} \\ i_L \\ v_{C_2} \end{bmatrix}}_{\mathbf{x}} + \underbrace{\begin{bmatrix} \frac{1}{C_1} \\ 0 \\ 0 \end{bmatrix}}_{\mathbb{B}_{\mathbf{on}}} \underbrace{\begin{bmatrix} i_{pv} \end{bmatrix}}_{\mathbf{w}} \tag{4}$$

$$\underbrace{\begin{bmatrix} v_{pv} \end{bmatrix}}_{\mathbf{y}_1} = \underbrace{\begin{bmatrix} 1 & 0 & 0 \end{bmatrix}}_{\mathbb{C}_{\mathbf{on}}} \underbrace{\begin{bmatrix} v_{pv} \\ i_L \\ v_{C_2} \end{bmatrix}}_{\mathbf{x}} \tag{5}$$

Similarly, the state-space model for operation in Mode 2 of the stated converter, in compact vector-matrix form, can be expressed as follows:

$$\underbrace{\begin{bmatrix} \dot{v}_{pv} \\ \dot{i}_L \\ \dot{v}_{C_2} \end{bmatrix}}_{\dot{\mathbf{x}}} = \underbrace{\begin{bmatrix} 0 & 0 & 0 \\ 0 & 0 & -\frac{1}{L} \\ 0 & \frac{1}{C_2} & -\frac{1}{R_L C_2} \end{bmatrix}}_{\mathbb{A}_{\mathbf{off}}} \underbrace{\begin{bmatrix} v_{pv} \\ i_L \\ v_{C_2} \end{bmatrix}}_{\mathbf{x}} + \underbrace{\begin{bmatrix} \frac{1}{C_1} \\ 0 \\ 0 \end{bmatrix}}_{\mathbb{B}_{\mathbf{off}}} \underbrace{\begin{bmatrix} i_{pv} \end{bmatrix}}_{\mathbf{w}} \tag{6}$$

$$\underbrace{\begin{bmatrix} v_{pv} \end{bmatrix}}_{\mathbf{y}_2} = \underbrace{\begin{bmatrix} 1 & 0 & 0 \end{bmatrix}}_{\mathbb{C}_{\mathbf{off}}} \underbrace{\begin{bmatrix} v_{pv} \\ i_L \\ v_{C_2} \end{bmatrix}}_{\mathbf{x}} \tag{7}$$

In Equations (4)–(7), $\mathbb{A}_{\mathbf{on}}$ and $\mathbb{A}_{\mathbf{off}}$ are the system matrices, $\mathbb{B}_{\mathbf{on}}$ and $\mathbb{B}_{\mathbf{off}}$ are the input column vectors and $\mathbb{C}_{\mathbf{on}}$ and $\mathbb{C}_{\mathbf{off}}$ are the output row vectors for Mode 1 and 2, respectively. Moreover, $\mathbf{x}$ is the state-variable vector indicating the input and output capacitor voltages and inductor current, $\mathbf{w}$ is the input disturbance vector representing the source (PV array) current, and $\mathbf{y}$ is the output vector denoting the PV array output voltage.

Now taking the weighted averages of $\mathbb{A}_{\mathbf{on}}$ and $\mathbb{A}_{\mathbf{off}}$, $\mathbb{B}_{\mathbf{on}}$ and $\mathbb{B}_{\mathbf{off}}$, and $\mathbb{C}_{\mathbf{on}}$ and $\mathbb{C}_{\mathbf{off}}$ with an appropriate duty ratio, d, as follows:

$$\left.\begin{aligned} \mathbb{A} &= (\mathbf{d})\mathbb{A}_{\mathbf{on}} + (\mathbf{1}-\mathbf{d})\mathbb{A}_{\mathbf{off}} \\ \mathbb{B} &= (\mathbf{d})\mathbb{B}_{\mathbf{on}} + (\mathbf{1}-\mathbf{d})\mathbb{B}_{\mathbf{off}} \\ \mathbb{C} &= (\mathbf{d})\mathbb{C}_{\mathbf{on}} + (\mathbf{1}-\mathbf{d})\mathbb{C}_{\mathbf{off}} \end{aligned}\right\} \tag{8}$$

Now, the state-space averaged discrete-time bilinear equivalent circuit model of the CCNI-BuBo converter can be expressed as follows:

$$\begin{aligned} \underbrace{\begin{bmatrix} \dot{v}_{pv} \\ \dot{i}_L \\ \dot{v}_{C_2} \end{bmatrix}}_{\dot{\mathbf{x}}} &= \underbrace{\begin{bmatrix} 0 & 0 & 0 \\ 0 & 0 & -\frac{1}{L} \\ 0 & \frac{1}{C_2} & -\frac{1}{R_L C_2} \end{bmatrix}}_{\mathbb{A}_{off}=\mathbb{A}_{\mathbf{c}}} \underbrace{\begin{bmatrix} v_{pv} \\ i_L \\ v_{C_2} \end{bmatrix}}_{\mathbf{x}} + \underbrace{\left(\underbrace{\begin{bmatrix} 0 & -\frac{1}{C_1} & 0 \\ \frac{1}{L} & 0 & 0 \\ 0 & 0 & -\frac{1}{R_L C_2} \end{bmatrix}}_{\mathbb{A}_{\mathbf{on}}} - \underbrace{\begin{bmatrix} 0 & 0 & 0 \\ 0 & 0 & -\frac{1}{L} \\ 0 & \frac{1}{C_2} & -\frac{1}{R_L C_2} \end{bmatrix}}_{\mathbb{A}_{\mathbf{off}}} \right)}_{\mathbb{B}_{cb}} \\ &\underbrace{\begin{bmatrix} v_{pv} \\ i_L \\ v_{C_2} \end{bmatrix}}_{\mathbf{x}} d(t) + \underbrace{\left(\underbrace{\begin{bmatrix} \frac{i_{pv}}{C_1} \\ 0 \\ 0 \end{bmatrix}}_{\mathbb{B}_{\mathbf{on}}\mathbf{w}} - \underbrace{\begin{bmatrix} \frac{i_{pv}}{C_1} \\ 0 \\ 0 \end{bmatrix}}_{\mathbb{B}_{\mathbf{off}}\mathbf{w}} \right)}_{\mathbb{B}_{\mathbf{c}}} d(t) + \underbrace{\begin{bmatrix} \frac{1}{C_1} \\ 0 \\ 0 \end{bmatrix}}_{\mathbb{B}_{\mathbf{off}}} \underbrace{\begin{bmatrix} i_{pv} \end{bmatrix}}_{\mathbf{w}} \end{aligned} \tag{9}$$

Since, $\mathbb{A}_{\mathbf{on}} \neq \mathbb{A}_{\mathbf{off}}$, hence the state-space averaged discrete-time equivalent circuit model of the CCNI-BuBo converter, expressed in Equation (9), is bilinear. It can be simplified as follows:

$$\dot{\mathbf{x}} = \mathbb{A}_{\mathbf{off}}\,\mathbf{x} + \underbrace{(\mathbb{A}_{\mathbf{on}} - \mathbb{A}_{\mathbf{off}})}_{\mathbb{B}_{\mathbf{cb}}}\,\mathbf{x}\,\mathbf{d} + \underbrace{\mathbb{B}_c\, d(t)}_{\mathbb{B}_{\mathbf{u}}} + \underbrace{\mathbb{B}_{\mathbf{off}}\,\mathbf{w}}_{\mathbb{B}_{\mathbf{w}}} \tag{10}$$

Equation (10) is in the form of a standard bilinear continuous-time system, where $d(t) = u(t)$ indicates the input to the system, $\mathbb{B}_{\mathbf{cb}}$ is the matrix of the bilinear terms $(\mathbf{x},\ \mathbf{d})$, $\mathbb{B}_{\mathbf{w}}$ is the matrix of input disturbances and $\mathbb{B}_{\mathbf{u}}$ is the matrix of control inputs.

Let, $v_{pv} = v_{C_1} = x_1$, $i_L = x_2$, and $v_{C_2} = v_R = x_3$. These notations will be used in the forthcoming sections. Different significant parameters of the CCNI-BuBo DC–DC converter are specified in Table 1.

5. Differential Flatness Based States Observer Design

Usually all the system state variables are available during the implementation of most of the control methodologies. However, some technical and economical constraints may inhibit the availability of the system states. An observer (or differentiator) can be employed for estimating the derivative of a missing/non-measurable system state variable. The main drawback of a (conventional) differentiator is that it increases the high frequency gain. Furthermore, a pure differentiator is not proper (or causal), and in case of a disturbance (e.g., a change or spike or noisy environment), it causes a theoretically infinite control signal. This phenomenon is termed as the chaos in the scientific literature. In general, a differentiator may either be exact or robust alone, but not both simultaneously. It requires a trade-off between exactness and robustness to simultaneously offer both with respect to the input noises and possible measurement errors [31]. For this reason, in this article, both the essential features are integrated into a single differentiator that accurately estimates the system state variables. This stated differentiator is based on a generalized STA (GSTA) that uniformly demonstrates robustness as well as exactness with a finite-time convergence [32].

Such that, for an i^{th} differentiator, an estimation (or observation) error can be defined as follows:

$$\zeta_1 = x_i - \widehat{x}_i \tag{11}$$

where x_i and $\widehat{x}_i$ are the actual and the estimated (or observed) values of x, respectively. Moreover, the observed output states of the differentiator, in compact vector-matrix notation, can be expressed as follows:

$$\begin{bmatrix} \dot{\widehat{x}}_i \\ \dot{\widehat{x}}_{i+1} \end{bmatrix} = \begin{bmatrix} -c_i \phi_i\left(\zeta_i\right) \\ -c_{i+1}\phi_{i+1}\left(\zeta_i\right) \end{bmatrix} \begin{bmatrix} \widehat{x}_{i+1} \\ 0 \end{bmatrix} \tag{12}$$

where, $i = 1, 2, 3$, $\widehat{x}_{i+1}$ is the estimated value of x_{i+1}, and c_i and c_{i+1} are the positive design constants. Since, the system under consideration possesses three state variables (x_1, x_2 and x_3), hence, using the stated strategy in Equation (12) $\widehat{x}_1$, $\widehat{x}_2$ and $\widehat{x}_3$ are obtained from a set of three differentiators, respectively.

The terms, $\phi_i\left(\zeta_i\right)$ and $\phi_{i+1}(\zeta_i)$, appearing in Equation (12), are defined as follows:

$$\phi_i(\zeta_i) = |\zeta_i|^{\frac{1}{2}} sign(\zeta_i) + \lambda |\zeta_i|^{\frac{3}{2}} sign(\zeta_i) \tag{13}$$

and

$$\phi_{i+1}(\zeta_i) = \frac{1}{2} sign(\zeta_i) + 2\lambda\zeta_i + \frac{3}{2}\lambda^2 |\zeta_i|^2 sign(\zeta_i) \tag{14}$$

where, $\lambda \geq 0$ is a scalar quantity. Putting $\lambda = 0$ in Equation (13) and (14) recovers the standard robust exact differentiator, via the SMC technique, as proposed in [31]. The higher-degree terms, that is, $|\zeta_i|^{\frac{3}{2}} sign(\zeta_i)$ and $|\zeta_i|^2 sign(\zeta_i)$, provide the differentiator with a uniform convergence. It means that the convergence time of the differentiator will be bounded by a constant. Moreover, it will be independent of any initial conditions.

Note that the tuning parameters (c_1, c_2 and λ) of the three GSTA based differentiators and their convergence analysis, using standard test input signals are given in Table A1 and Figures A1 and A2, in Appendix A, respectively.

Differential Flatness Approach

The flatness concept has been derived from the differential algebra. In nonlinear control system theory, a flat system is the one that is equivalent to a linear system. In other words, the system dynamics render the ability to support an accurate linearization. This linearization process is supported by a special dynamic feedback mechanism called the endogenous feedback. A system satisfying the flatness property is termed as a differentially-flat system or simply flat system. One major property of a flat system is that the system states and the input variables can be written directly, (without requiring any integration of a differential equation), in terms of a particular set of variables called the flat (or linearized) outputs, along with a finite number of their derivatives [33]. In other words, without needing any integration, all the system state variables and inputs can be extracted from the flat outputs.

Once $\widehat{x}_1$, $\widehat{x}_2$ and $\widehat{x}_3$ are obtained from a set of three differentiators, in the next step, the differential flatness approach (DFA) is applied on these stated differentiators to recover the (actual) missing system states x_{2f} and x_{3f} from $\widehat{x}_1$, $\widehat{x}_2$, respectively. The implementation of the DFA is illustrated in Figure 5.

If

$$\begin{cases} v_{pv} = v_{C_1} = x_1 \\ i_L = x_2 \\ v_{C_2} = v_{R_L} = x_3 \\ d = u \end{cases}$$

Equation (9) can be re-written as follows:

$$\begin{cases} \dot{x}_1 = \dfrac{-ux_2}{C_1} + \dfrac{i_{pv}}{C_1} \\[2ex] \dot{x}_2 = \dfrac{ux_1}{L} + \dfrac{(u-1)\,x_3}{L} \\[2ex] \dot{x}_3 = \dfrac{(1-u)\,x_2}{C_2} - \dfrac{x_3}{R_L C_2} \end{cases}$$

Then, the DFA can be applied by rewriting the first two equations of the previous set of equations, as follows:

$$x_{2f} = \frac{C_1}{u}\left(-\dot{\widehat{x}}_1 + \frac{i_{pv}}{C_1}\right) \tag{15}$$

and

$$x_{3f} = \frac{L}{(u-1)}\left(-\frac{u\widehat{x}_1}{L} + \dot{\widehat{x}}_2\right) \tag{16}$$

Now, these two (actual) missing system states (i.e., x_{2f} and x_{3f}), recovered through the DFA, and called the flat or linearized (output) states, are applied as inputs to the differentiators. The Matlab/Simulink implementation of the DFA based states observer design along with the proposed MPPT strategy is illustrated in Figures 6 and 7.

6. Backstepping Based Super-Twisting Sliding Mode MPPT Control Design

This section covers the formulation of the nonlinear BSTSMC based MPPT paradigm for maximizing the power extraction from the PV array. Note that this design procedure uses the observed values of the system state variables (i.e., $\widehat{x}_1$, $\widehat{x}_2$ and $\widehat{x}_3$) instead of the actual (or true) states. The proposed MPPT controller constantly adjusts the duty cycle, d, of the CCNI-BuBo converter switches and adapts the PV system operating point (MPP or V_{MPP}) to the varying atmospheric conditions, thus ensuring the optimal power extraction from it.

The proposed BSTSMC law is composed of the backstepping based equivalent control law, u_{eq}, and the super-twisting sliding mode based discontinuous control law, u_{disc}.

6.1. The Backstepping Based Equivalent Control Law

The backstepping based equivalent control law is designed in the following two step:

Step 1:

The proposed control system design is initiated by defining the PV array output voltage tracking error, ϵ_1, as follows:

$$\epsilon_1 = \widehat{v}_{pv} - v^r_{pv} = \widehat{x}_1 - x^r_1 \tag{17}$$

In Equation (17), $\widehat{x}_1$ is the PV array observed output voltage and $x^r_1 = v^r_{pv}$ is the reference (or desired) output voltage, that must be tracked by $\widehat{x}_1$. The goal is to drive the error ϵ_1 to the origin (equilibrium point), O, asymptotically.

Differentiating Equation (17) with respect to time, and substituting $\dot{v}_{pv} = \widehat{x}_1$ from Equation (9), it yields:

$$\dot{\epsilon}_1 = \dot{\widehat{v}}_{pv} - \dot{v}^r_{pv} = \dot{\widehat{x}}_1 - \dot{x}^r_1 = -\frac{u\widehat{x}_2}{C_1} + \frac{i_{pv}}{C_1} - \dot{x}^r_1 \tag{18}$$

For guaranteeing the convergence of the error ϵ_1 to the equilibrium point, selecting a Lyapunov function candidate, V_{f1}, that must satisfy three conditions, namely: (i) V_{f1} must be positive definite (ii) V_{f1} must be radially unbounded, and (iii) V_{f1} must have a negative definite time derivative, in order to guarantee the local asymptotic stability of the system [34,35].

The selected Lyapunov function, V_{f1}, along with its time derivative, $\dot{V}_{f1}$, are expressed in Equation (19) and (20), respectively, as follows:

$$V_{f1} = \frac{1}{2}\epsilon_1^2 \tag{19}$$

and

$$\dot{V}_{f1} = \epsilon_1\dot{\epsilon}_1 = \epsilon_1\left(-\frac{u\widehat{x}_2}{C_1} + \frac{i_{pv}}{C_1} - \dot{x}^r_1\right) \tag{20}$$

For $\dot{V}_{f1}$ to be negative definite, the following condition must be satisfied:

$$\left(-\frac{u\widehat{x}_2}{C_1} + \frac{i_{pv}}{C_1} - \dot{x}^r_1\right) = -\kappa_1\epsilon_1 \tag{21}$$

where κ_1 is a positive design constant.

Substituting Equation (21) into (20) yields:

$$\dot{V}_{f1} = \epsilon_1\dot{\epsilon}_1 = \epsilon_1\left(-\frac{u\widehat{x}_2}{C_1} + \frac{i_{pv}}{C_1} - \dot{x}^r_1\right) = -\kappa_1\epsilon_1^2 \tag{22}$$

Suppose the second state of the system, that is, the inductor current, $\widehat{i}_L = \widehat{x}_2$, be a virtual control input [15,16]. Then the stabilization function, say β , that serves as a reference (or desired) current for the inductor current, $\hat{x}_2$, can be obtained by equating Equations (20) and (22) and then deducing $\hat{x}_2 = \beta$ as follows:

$$\beta = \frac{1}{u}\left(C_1\kappa_1\epsilon_1 + i_{pv} - C_1\dot{x}_1^r\right) \tag{23}$$

Step 2:

To track $\hat{x}_2$ to its reference β, another error, ϵ_2, is defined as follows:

$$\left.\begin{aligned} \epsilon_2 &= \hat{x}_2 - \beta \\ \text{or} \quad \hat{x}_2 &= \epsilon_2 + \beta \end{aligned}\right\} \tag{24}$$

Substituting $\hat{x}_2$, from Equation (24) into (18) and then simplifying by substituting β from Equation (23), it yields:

$$\dot{\epsilon}_1 = -\frac{u(\epsilon_2+\beta)}{C_1} + \frac{i_{pv}}{C_1} - \dot{x}_1^r = -\kappa_1\epsilon_1 - \frac{u\epsilon_2}{C_1} \tag{25}$$

Substituting Equation (25) into (20), it yields:

$$\dot{V}_{f1} = -\kappa_1\epsilon_1^2 - \frac{u\epsilon_1\epsilon_2}{C_1} \tag{26}$$

Applying the quotient rule of derivatives, calculating the time derivative of Equation (23) and simplifying by substituting β from Equation (23) and $\dot{\epsilon_1}$ from Equation (25), it gives:

$$\dot{\beta} = \frac{1}{u}\left[-C_1\kappa_1^2\epsilon_1 + \dot{i}_{pv} - C_1\ddot{x}_1^r\right] - \kappa_1\epsilon_2 - \frac{\dot{u}\beta}{u} \tag{27}$$

Taking the time derivative of ϵ_2 in Equation (24) gives: $\dot{\epsilon}_2 = \dot{\hat{x}}_2 - \dot{\beta}$, and substituting $\dot{\hat{x}}_2 = \dot{\hat{i}}_L$ and $\dot{\beta}$ from Equations (9) and (27), respectively, it gives:

$$\dot{\epsilon}_2 = \frac{u\hat{x}_1}{L} + \frac{(u-1)\hat{x}_3}{L} - \frac{1}{u}\left(-C_1\kappa_1^2\epsilon_1 + \dot{i}_{pv} - C_1\ddot{x}_1^r\right) + \kappa_1\epsilon_2 + \frac{\dot{u}\beta}{u} \tag{28}$$

Now, selecting another composite Lyapunov function candidate, V_{f2}, that will guarantee the convergence of both the errors ϵ_1 and ϵ_2, as well as the asymptotic stability of the system to the equilibrium point, under the same assumptions as those made for V_{f1} [34,35].

This newly selected Lyapunov function, V_{f2}, along with its time derivative, $\dot{V}_{f2}$, are expressed in Equations (29) and (30), respectively, as follows:

$$V_{f2} = V_{f1} + \frac{1}{2}\epsilon_2^2 \tag{29}$$

and

$$\begin{aligned}\dot{V}_{f2} = \dot{V}_{f1} + \epsilon_2\dot{\epsilon}_2 = -\kappa_1\epsilon_1^2 + \epsilon_2\Bigg[&\frac{u\hat{x}_1}{L} + \frac{(u-1)\hat{x}_3}{L} - \frac{1}{u}\left(-C_1\kappa_1^2\epsilon_1 + \dot{i}_{pv} - C_1\ddot{x}_1^{ref}\right) + \\ &\kappa_1\epsilon_2 + \frac{\dot{u}\beta}{u} - \frac{u\epsilon_1}{C_1}\Bigg]\end{aligned} \tag{30}$$

For $\dot{V}_{f2}$ to be negative definite, the following condition must be satisfied:

$$\dot{V}_{f2} = -\kappa_1\epsilon_1^2 - \kappa_2\epsilon_2^2 \tag{31}$$

where both κ_1 and κ_2 are positive design constants.

Now, comparing Equations (30) and (31) and working out $\dot{u}$, it gives:

$$\dot{u} = -\frac{u}{\beta}\left[\kappa_2\epsilon_2 + \frac{u\hat{x}_1}{L} + \frac{(u-1)\hat{x}_3}{L} - \frac{1}{u}\left(-C_1\kappa_1^2\epsilon_1 + \dot{i}_{pv} - C_1\ddot{x}_1^{ref}\right) + \kappa_1\epsilon_2 - \frac{u\epsilon_1}{C_1}\right] \tag{32}$$

Simplifying Equation (32) it yields the backstepping based equivalent control law, u_{eq}, as follows:

$$\dot{u}_{eq} = \frac{1}{\beta}\left[-\epsilon_2\left(\kappa_1+\kappa_2\right)u - \epsilon_1\left(C_1\kappa_1^2 - \frac{u^2}{C_1}\right) - \frac{u^2\widehat{x}_1}{L} - \frac{u(u-1)\widehat{x}_3}{L} + \dot{i}_{pv} - C_1\ddot{x}_1^r\right] \tag{33}$$

where $\beta \neq 0$.

6.2. The Super-Twisting Sliding Mode Based Discontinuous Control Law

Now, the super-twisting sliding mode based discontinuous control law, u_{disc}, is designed as follows [18]:

$$\dot{u}_{disc} = -\kappa_3\sqrt{|\epsilon_1|}sign\left(\epsilon_1\right) - \kappa_4\int sign\left(\epsilon_1\right)dt \tag{34}$$

where κ_3 and κ_4 are positive design constants.

6.3. The Proposed Mppt Control Law

Finally, the proposed BSTSMC based MPPT law, u_T, is given as follows:

$$\begin{aligned}\dot{u}_T = \dot{u}_{eq} + \dot{u}_{disc} = -\kappa_3\sqrt{|\epsilon_1|}sign\left(\epsilon_1\right) - \kappa_4\int sign\left(\epsilon_1\right)dt + \frac{1}{\beta}\Bigg[-\epsilon_2\left(\kappa_1+\kappa_2\right)u - \epsilon_1\left(C_1\kappa_1^2 - \frac{u^2}{C_1}\right)\\ - \frac{u^2\widehat{x}_1}{L} - \frac{u(u-1)\widehat{x}_3}{L} + \dot{i}_{pv} - C_1\ddot{x}_1^r\Bigg]\end{aligned} \tag{35}$$

Different design constants of the BSTSMC law (i.e., κ_1, κ_2, κ_3 and κ_4) are expressed in Table 1. In Equation (35), $(0 < u_T < 1)$. As $\lim_{t\to\infty} v_{pv} = V_{MPP}$. In the same way, as $\lim_{t\to\infty} P_{pv} = P_{MPP}$. Note that the proposed BSTSMC based MPPT law, u_T, constantly adjusts the duty cycle, d, of the CCNI-BuBo converter switches, S_1 and S_2, as shown in Figure 5, and adapts the PV system operating point (MPP or V_{MPP}) to the varying atmospheric conditions, thus maximizing its power output.

The implementation of the BSTSMC based MPPT law, u_T is illustrated in Figure 8, where each step includes the dynamics of the previous subsystem(s). The Matlab/Simulink implementation of the proposed MPPT strategy along with the DFA based states observer strategy is illustrated in Figures 6 and 7.

Note that the stability analysis of the zero dynamics state, x_3, is given in Figures A3 and A4 in Appendix B.

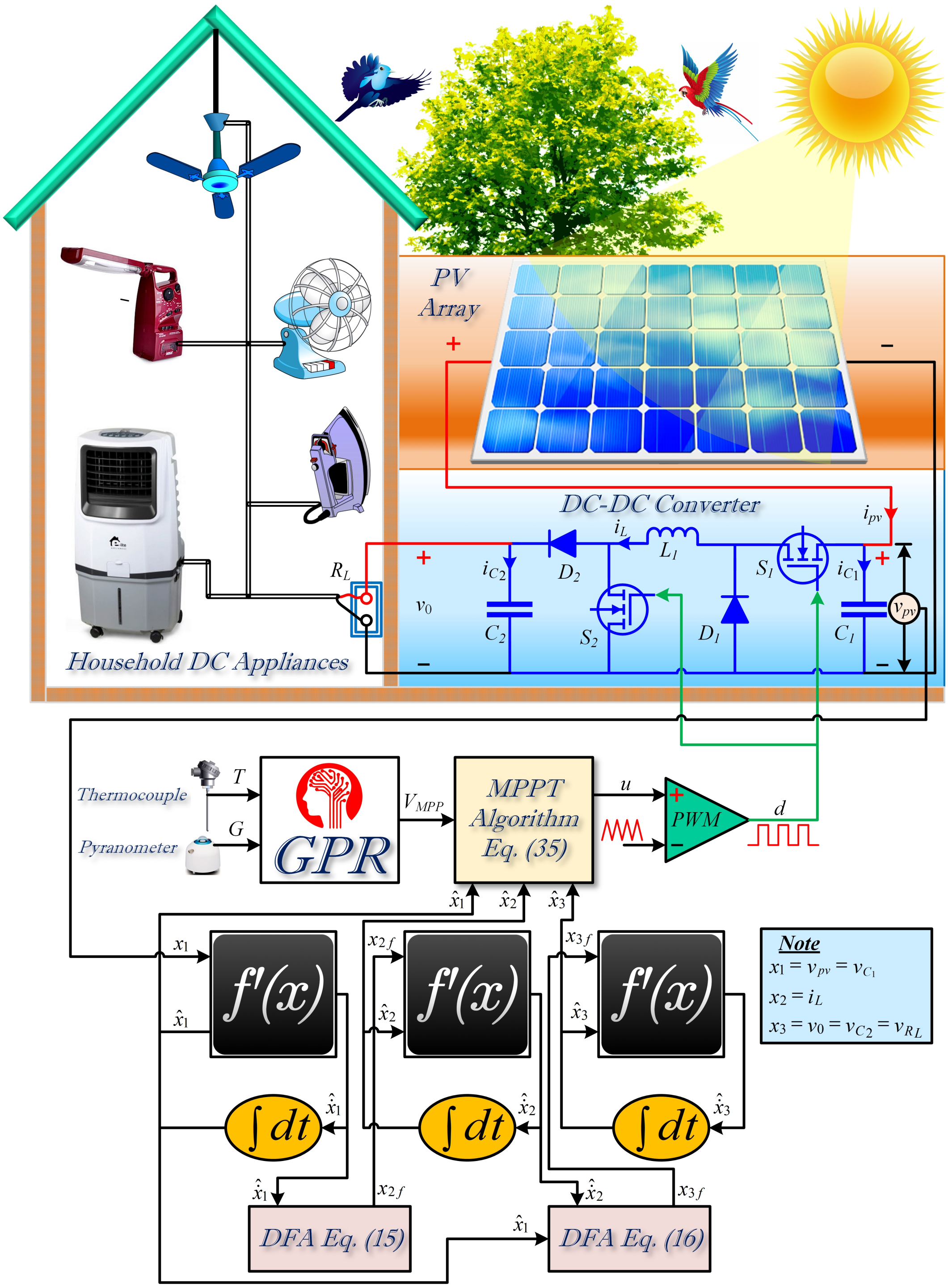

Figure 5. The overall closed-loop control system for the proposed maximum power point tracking (MPPT) strategy.

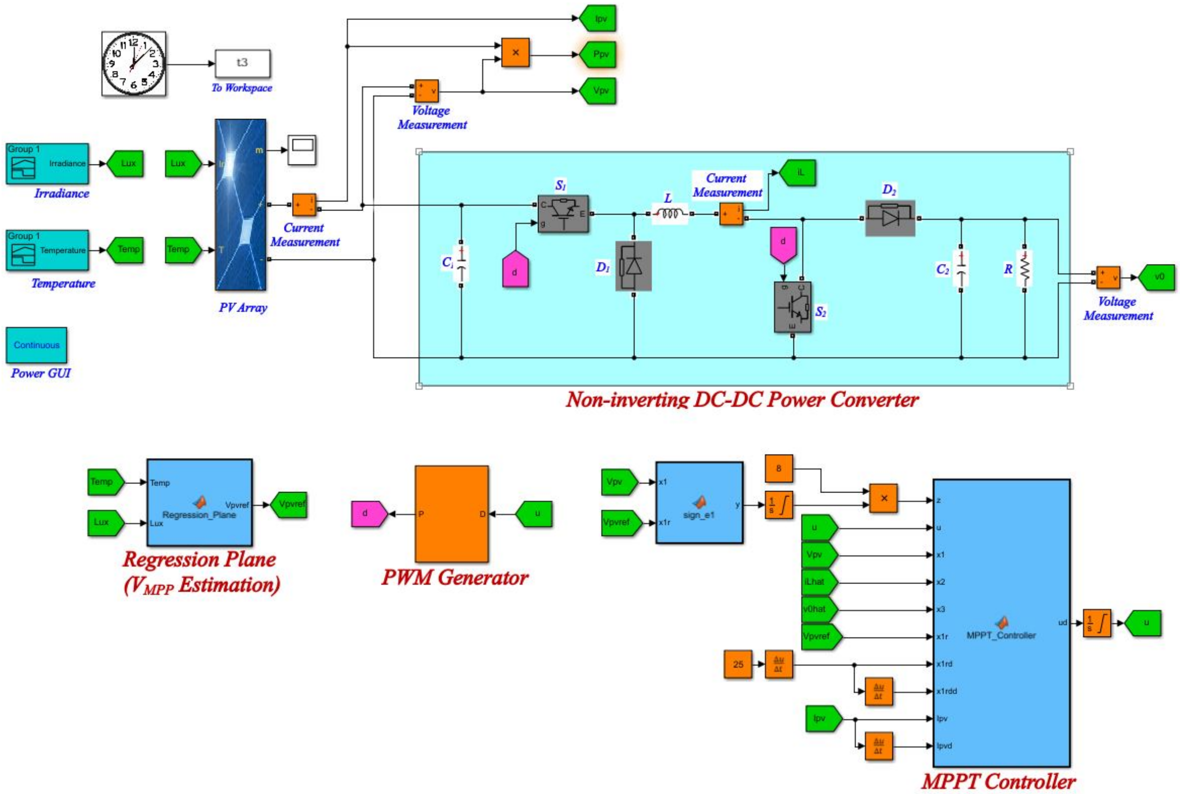

Figure 6. Matlab/Simulink model of the proposed MPPT scheme with main parts.

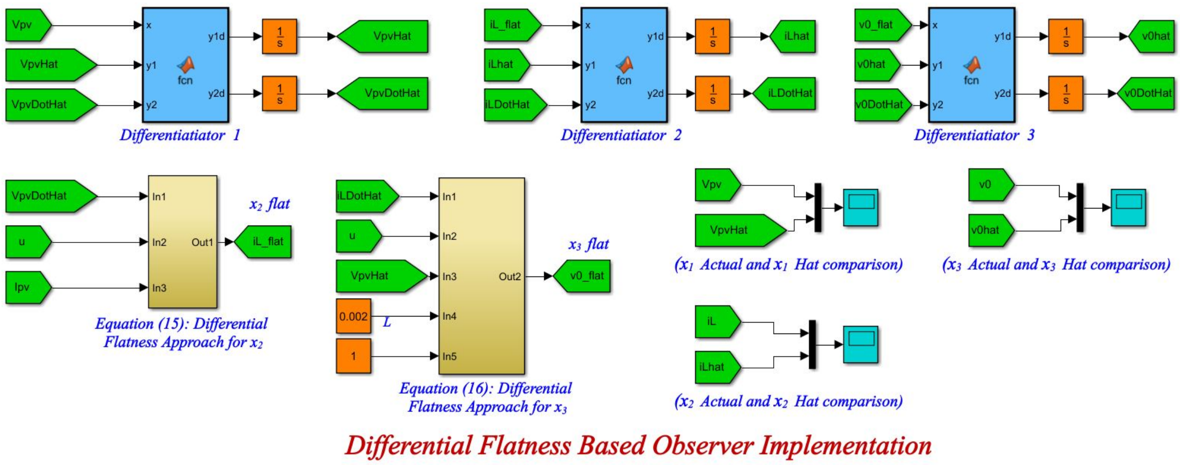

Figure 7. Matlab/Simulink model of the proposed differential flatness based states observer.

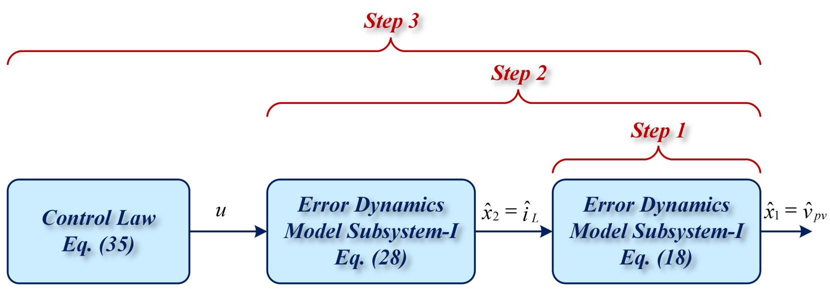

Figure 8. Block diagram for implementation of three-step backstepping super-twisting sliding mode control (BSTSMC) based MPPT law.

Table 1. Complete parameters of the PV system.

Name	Quantity	Value	
PV Array	Series cells/PV module	72	
	Parallel cells/PV module	1	
	No. of modules/PV string	4	
	No. of strings/PV array	4	
	No. of modules/PV array	16	
	Single module output power	1555 W	@STC
	PV array output power	24.880 W	@STC
	Module voltage at MPP	102.60 V	@STC
	Module current at MPP	15.16 A	@STC
	Module open-circuit voltage	165.80 V	@STC
	Module short-circuit current	17.56 A	@STC
DC–DC Converter	Input capacitor, C_1	1 mF	
	Output capacitor, C_2	48 µF	
	Inductor, L	2 mH	
	MOSFET Switching frequency, f_{sw}	5 kHz	
	Load resistance, R_L	50, 40, 60 Ω	
Controller (BSTSMC)	Constant, κ_1	100	
	Constant, κ_2	100,000	
	Constant, κ_3	4	
	Constant, κ_4	8	

7. MPPT Performance Evaluation in Matlab/Simulink

This section covers the performance validation of the proposed MPPT controller in Matlab/Simulink platform under five different case studies, described below:

Case 1: Performance evaluation test under simultaneous variation of the temperature, irradiance and load

Case 2: Performance evaluation test for robustness against faults under simultaneous variation of the temperature, irradiance and load

Case 3: Performance evaluation test for robustness against plant parametric uncertainties under simultaneous variation of the temperature, irradiance and load

Case 4: Performance comparison with conventional MPPT schemes under simultaneous variation of the temperature, irradiance and load

Case 5: Performance comparison with conventional MPPT schemes for robustness against faults under simultaneous variation of the temperature, irradiance and load

The total simulation time, t, is chosen to be short (i.e., 0.3 s) for each case study to indicate the fast response time of the proposed MPPT controller. The overall simulation time is further subdivided into three equal time intervals of 0.1 s each. Moving from one sub-interval of time to another, the temperature, irradiance and load resistance are varied in a quick succession as follows:

- Sub-interval 1 ($0 \rightarrow 0.1$ s): (25 °C, 1000 W/m^2, 50 Ω)
- Sub-interval 2 ($0.1 \rightarrow 0.2$ s: (65 °C, 850 W/m^2, 40 Ω)
- Sub-interval 3 ($0.2 \rightarrow 0.3$ s): (25 °C, 650 W/m^2, 60 Ω)

The temperature and irradiance profiles are illustrated in Figure 9.

The simulation with and without states observer was run on a computing machine with Intel(R) Core (TM) i5-6200 CPU @2.30 GHz (4 CPUs), ∼2.40 GHz, 8 GB RAM, 6th generation. On this system, a 0.3 s simulation took 20 s without flatness-based observer, and 20.001 23 s with flatness-based observer. It shows that the observer is computationally not costly and hence offers a negligible computational cost. Therefore, its implementation is highly justified in this application.

7.1. Performance Evaluation Test under Simultaneous Variation of the Temperature, Irradiance and Load

This test is carried out to evaluate the performance of the proposed MPPT technique under simultaneous variation of the atmospheric conditions and the load.

In Figure 10, the PV array output voltages are compared for the three MPPT candidates. It can be observed that the proposed BSTSMC based MPPT candidate offers a superior tracking performance with very a fast rise time, fast settling time and minute chattering. The conventional SMC strategy exhibits considerable chattering, while the backstepping strategy continuously renders steady-state error during MPP tracking. For change in the atmospheric conditions as well the load, after every 0.1 s, the proposed scheme performs the best by converging the PV array output voltage to its reference, V_{MPP}, earlier than the other two MPPT candidates. Similarly, Figure 11 illustrates the the PV array output powers comparison for each candidate MPPT strategy. Again, the proposed MPPT technique has the best tracking performance in terms of having faster rise time, faster convergence and minute chattering.

The actual and the observed system states are compared in Figure 12, from which it can be concluded that the GSTA based DFA is accurately retrieving the system states.

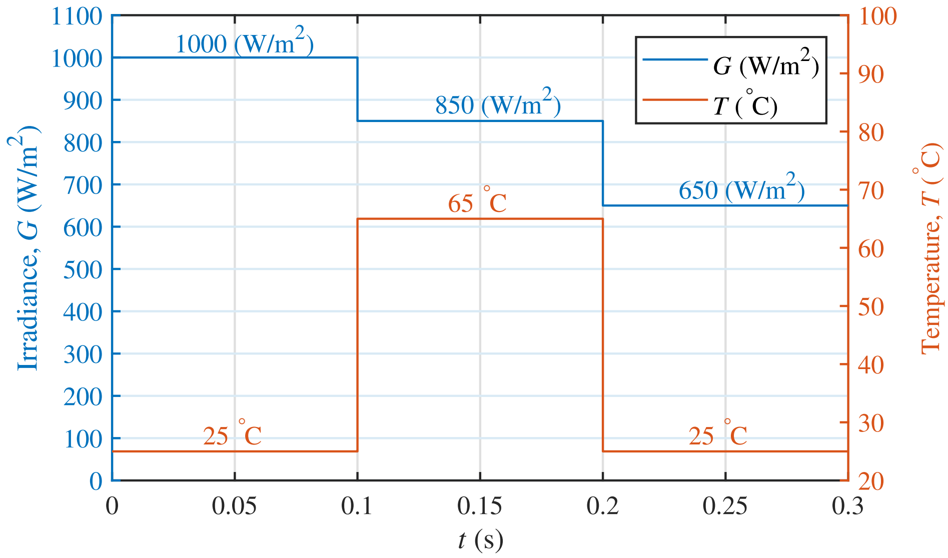

Figure 9. Irradiance and temperature profiles for MPPT controller.

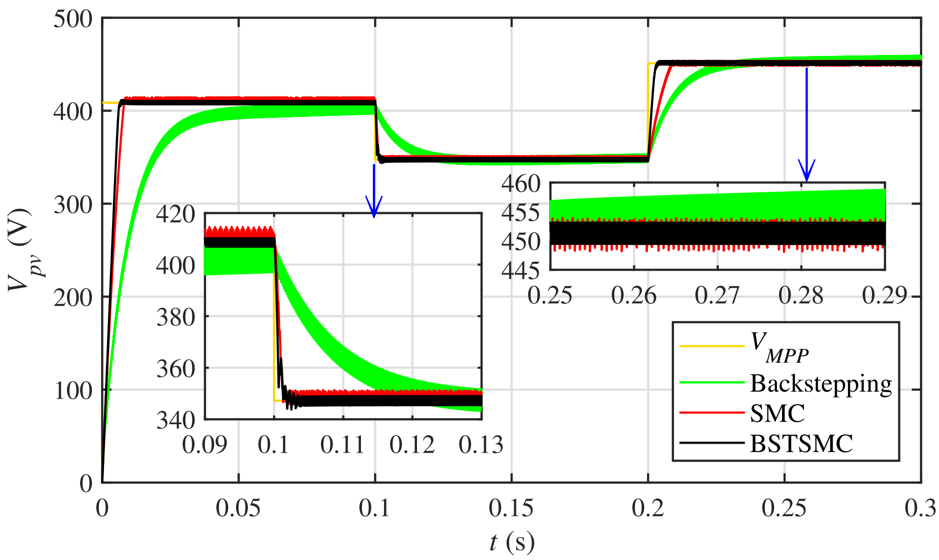

Figure 10. PV array output voltage comparison in Case 1.

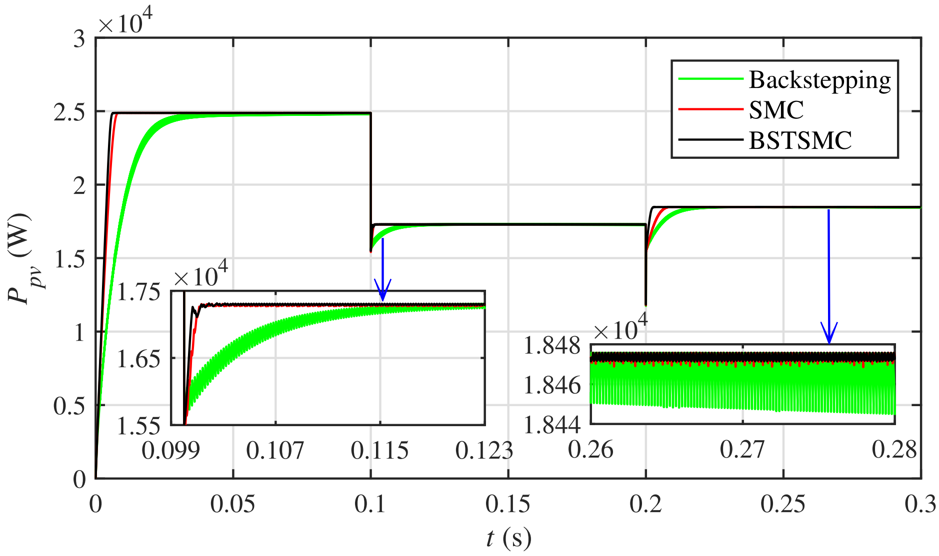

Figure 11. PV array output power comparison in Case 1.

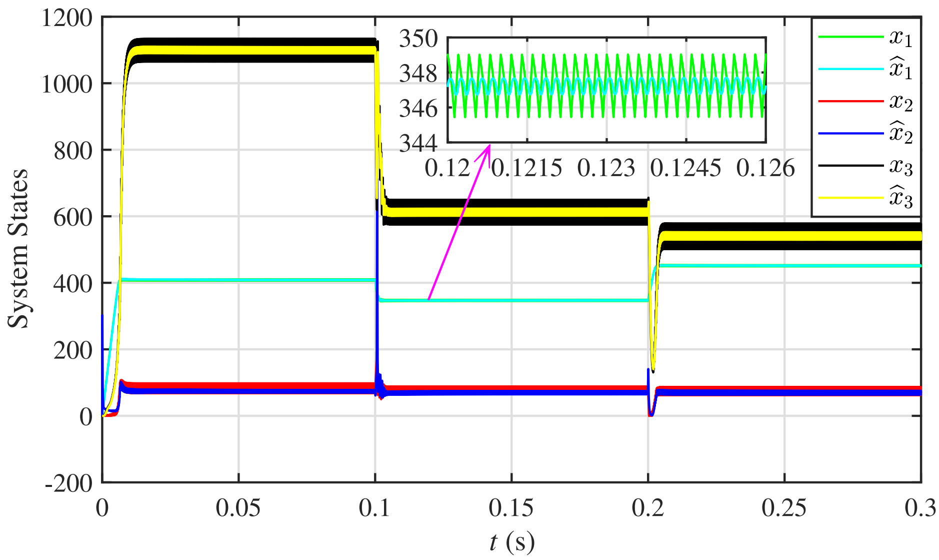

Figure 12. Actual and observed system states comparison in Case 1.

7.2. Performance Evaluation Test for Robustness against Faults under Simultaneous Variation of the Temperature, Irradiance and Load

In this test, the robustness of the proposed MPPT candidate is evaluated against multiple sinusoidal faults occurring in the CCNI-BuBo converter, under simultaneous variation of the environmental conditions and the load.

For this purpose, time-varying sinusoidal faults are injected into the DC–DC converter input and output voltages (i.e., $\widehat{x}_1$ and $\widehat{x}_3$, respectively). Under fault injections, $\widehat{x}_{1,new} = \widehat{x}_1 + \delta\widehat{x}_1 = \widehat{x}_1 + \frac{0.5u}{C_1} sin(t)$, and $\widehat{x}_{3,new} = \widehat{x}_3 + \delta\widehat{x}_3 = \widehat{x}_3 + \frac{55u}{C_1} sin(t)$. Furthermore, $\delta\widehat{x}_1$ remains active from 0.16–0.18 s only, while $\delta\widehat{x}_3$ from 0.06-0.08 s only.

For each MPPT candidate, the PV array output voltages, under faults, are compared in Figure 13. It is evident that at the onset of faults, both the backstepping and the conventional SMC schemes deviate from the V_{MPP}, thereby losing tracking. Rather, the SMC technique doesn't track the V_{MPP}, during the sub-interval 3 (0.2 $\rightarrow$ 0.3 s) with (25 °C, 650 W/m^2, 60 Ω). However, the proposed MPPT technique remains almost unaffected during faults and still tends to adequately keep tracking the V_{MPP}. This confirms the robustness of the proposed MPPT strategy against the injection of time-varying sinusoidal fault voltages in the PV array output voltage (i.e., converter input voltage) and converter output. Similarly, Figure 14, provides a comparison of the PV array output powers, under faults, for each MPPT candidate. Again, the proposed MPPT strategy remains almost unaffected in case of faults, while the other two MPPT strategies deviate from the P_{MPP}, thus losing tracking. Hence, it can be concluded that the proposed MPPT strategy is more robust than the other two MPP candidates. Figure 15 depicts a comparison of the actual and the observed system states under faults. It is evident that the GSTA based DFA is accurately observing the system states.

7.3. Performance Evaluation Test for Robustness against Plant Parametric Uncertainties under Simultaneous Variation of the Temperature, Irradiance and Load

This test covers the the sensitivity analysis of the proposed MPPT scheme against the plant (DC–DC converter) parametric uncertainties under simultaneous variation of the atmospheric conditions and the load.

For this purpose, parametric uncertainties are introduced into the inductor (L) and output capacitor (C_2) of the DC–DC converter. Such that L is increased by 25 times, while C_2 is decreased by 100 times with the end result: L_{new} = 50 mH and $C_{2,new}$ = 0.48 µF. Furthermore, L_{new} remains effective from 0.06–0.08 s only, while $C_{2,new}$ remains effective from 0.16–0.18 s only.

In Figure 16, the PV array output voltages are compared, under uncertainties, for each MPPT candidate. It can be seen that both the capacitive and inductive uncertainties greatly deteriorate the MPPT performance of the backstepping as well the conventional SMC techniques. However, the proposed MPPT technique shows more robustness by remaining almost unaffected during plant parametric uncertainties. Similarly, Figure 17 shows the PV array output powers comparison for each MPPT scheme, under plant parametric uncertainties. Again, it can be observed that the backstepping technique has the worst performance, while the proposed MPPT scheme has the best performance under parametric uncertainties. The actual and the observed system states are compared in Figure 18 under plant parametric uncertainties. It is evident that the GSTA based DFA is accurately estimating the system states.

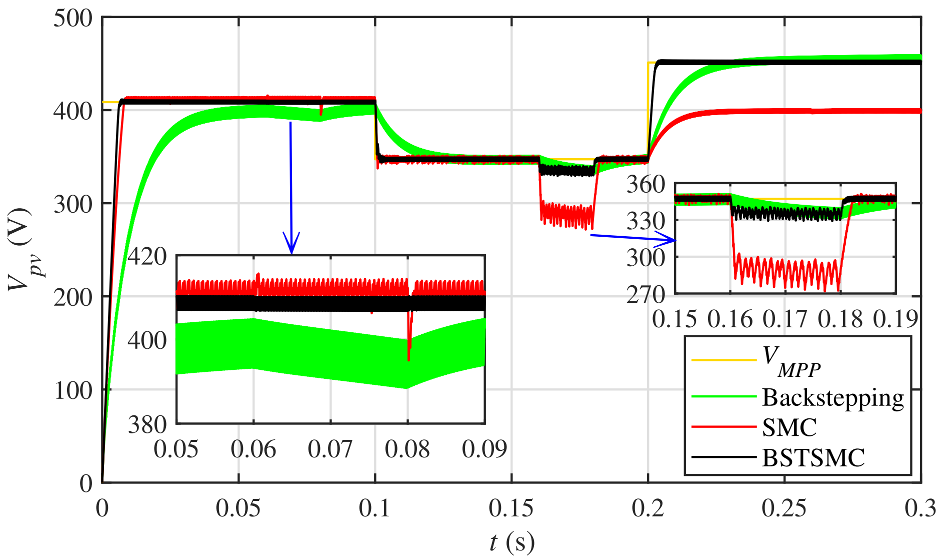

Figure 13. PV array output voltage comparison in Case 2.

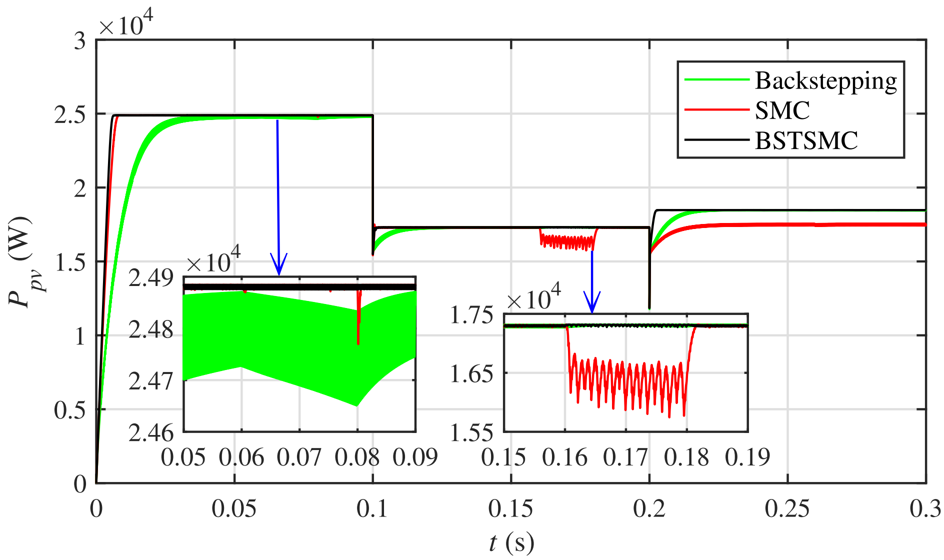

Figure 14. PV array output power comparison in Case 2.

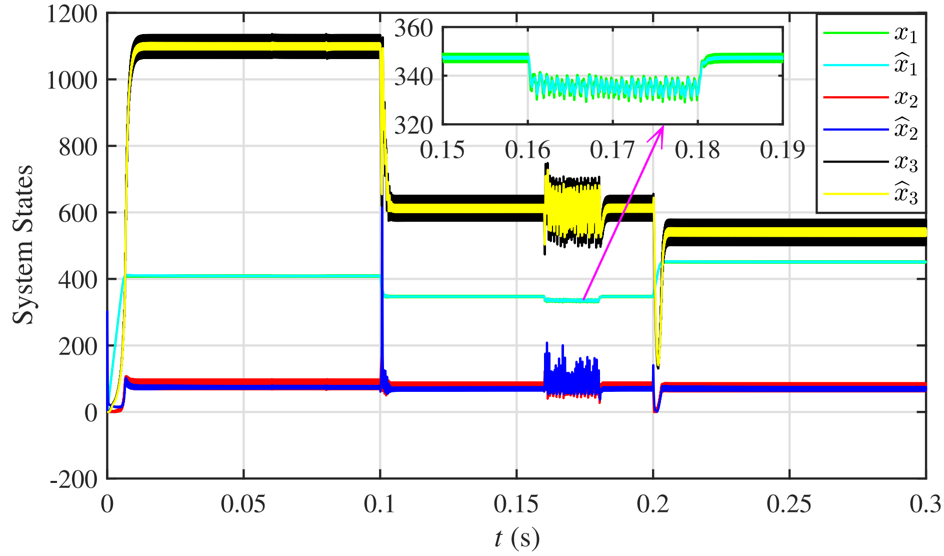

Figure 15. Actual and observed system states comparison in Case 2.

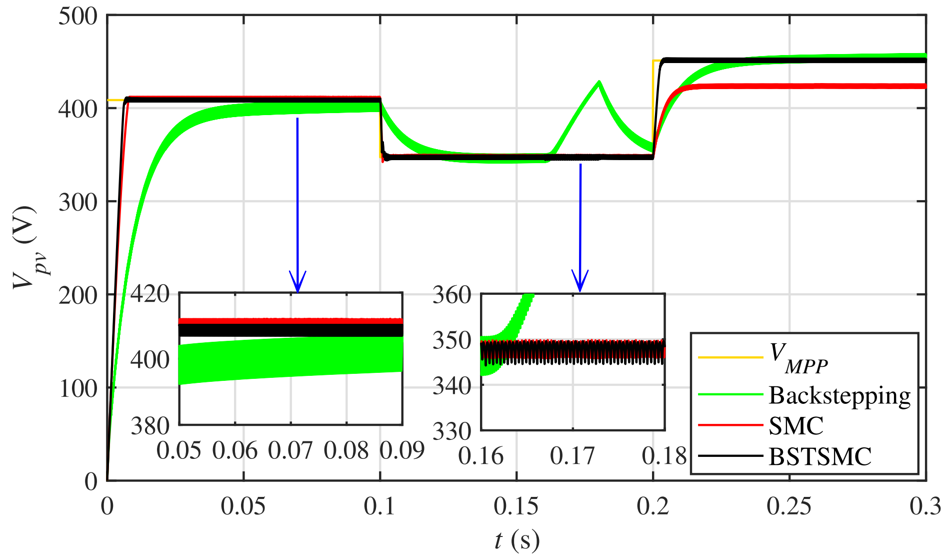

Figure 16. PV array output voltage comparison in Case 3.

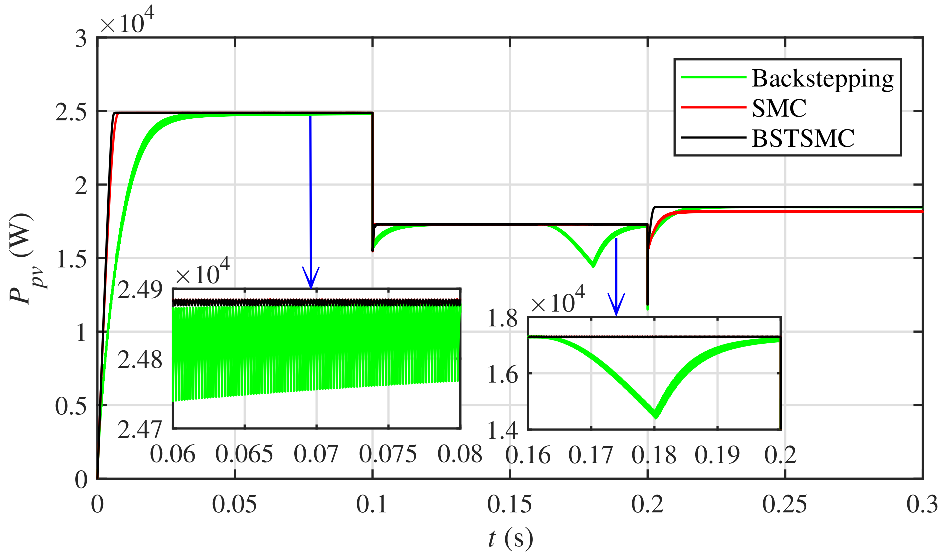

Figure 17. PV array output power comparison in Case 3.

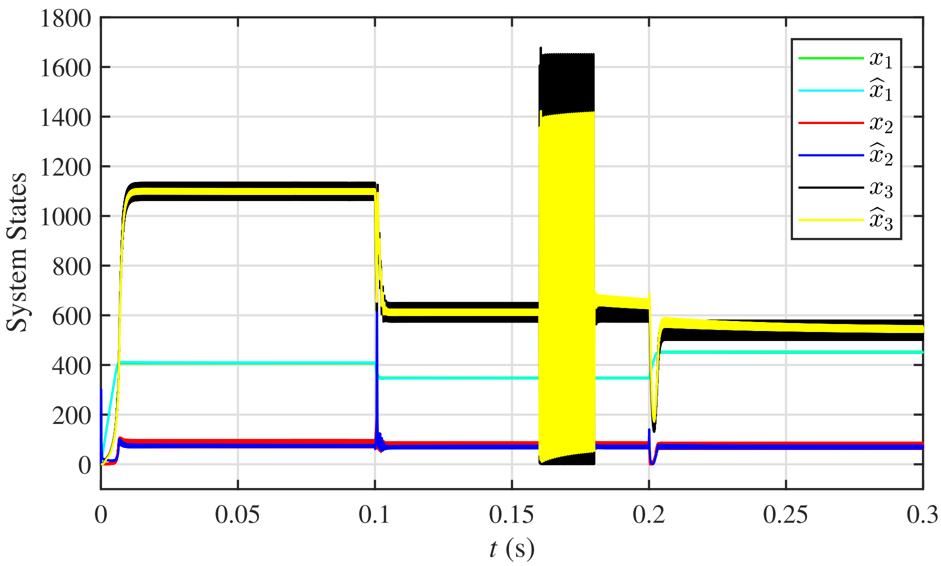

Figure 18. Actual and observed system states comparison in Case 3.

7.4. Performance Comparison with Conventional MPPT Schemes under Simultaneous Variation of the Temperature, Irradiance and Load

In this test, the effectiveness and MPPT performance of the proposed MPPT scheme is compared with the conventional PID and P&O based MPPT schemes, under simultaneous variation of the atmospheric conditions and the load.

The irradiance, temperature and load profiles are kept the same as previous. The PV array output voltages and powers comparison, shown in Figures 19 and 20, respectively, demonstrate that both the conventional PID and P&O based MPPT schemes exhibit a lot of oscillations around the V_{MPP} during their steady-states. This is practically undesirable. On the contrary, the proposed MPPT scheme offers the best MPPT performance, thus, completely outmatching the conventional MPPT techniques.

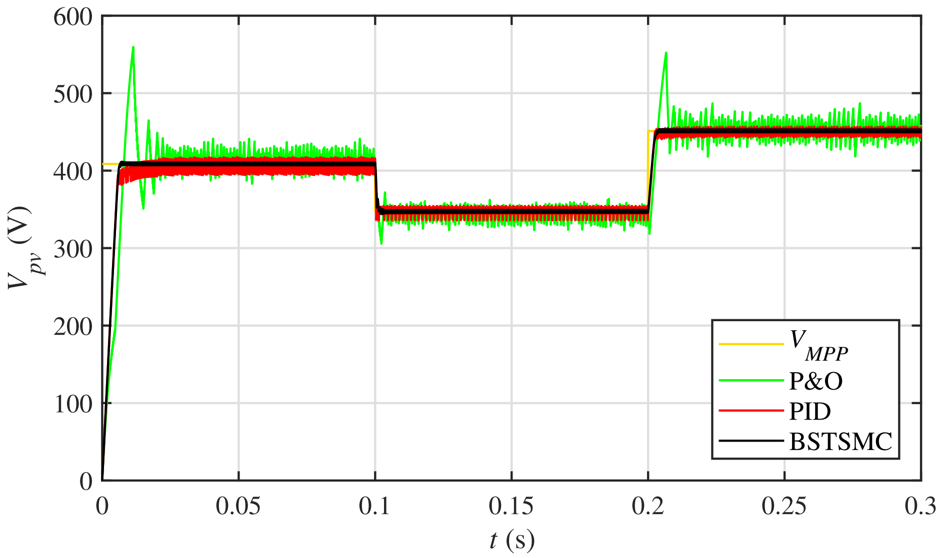

Figure 19. PV array output voltage comparison in Case 4.

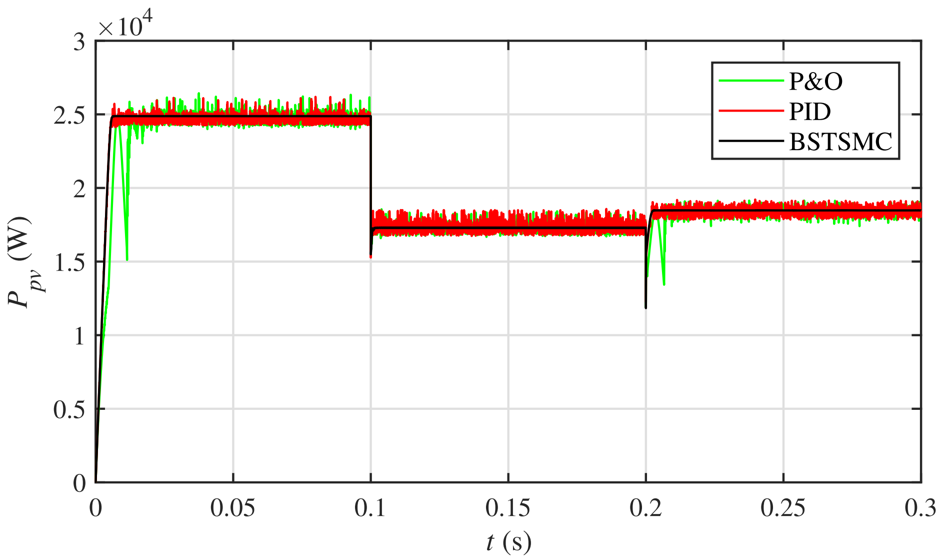

Figure 20. PV array output power comparison in Case 4.

7.5. Performance Comparison with Conventional MPPT Schemes for Robustness against Faults under Simultaneous Variation of the Temperature, Irradiance and Load

This test is carried out to further compare the effectiveness of the proposed MPPT strategy with the conventional PID and P&O based MPPT techniques, under faults and simultaneous variation of the atmospheric conditions and the load.

The load and atmospheric conditions profiles are the same as previous. Furthermore, the faults are the same as injected in Case 2. It is clear from the PV array output voltages and powers, depicted in Figures 21 and 22, respectively, that the proposed BSTSMC based MPPT strategy has the best MPPT performance and is much robust against faults than both of the conventional MPPT schemes.

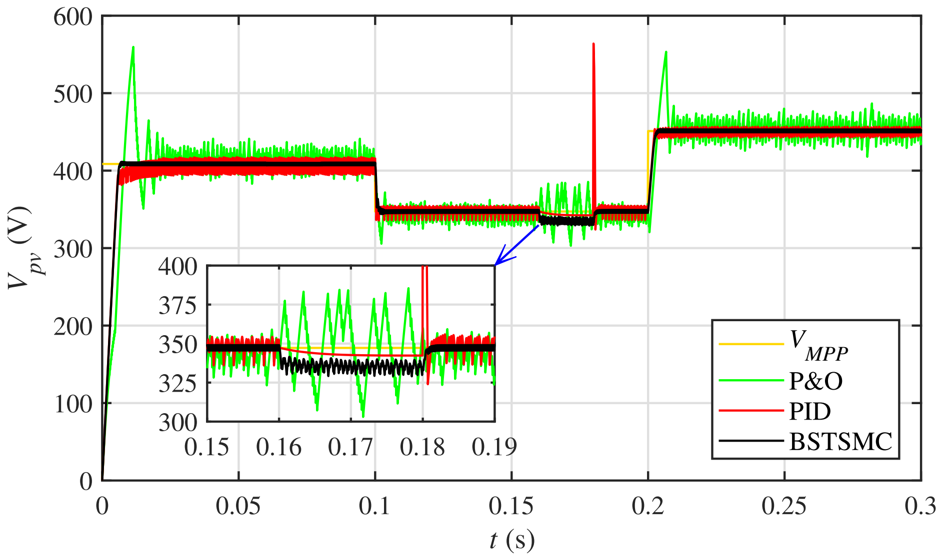

Figure 21. PV array output voltage comparison in Case 5.

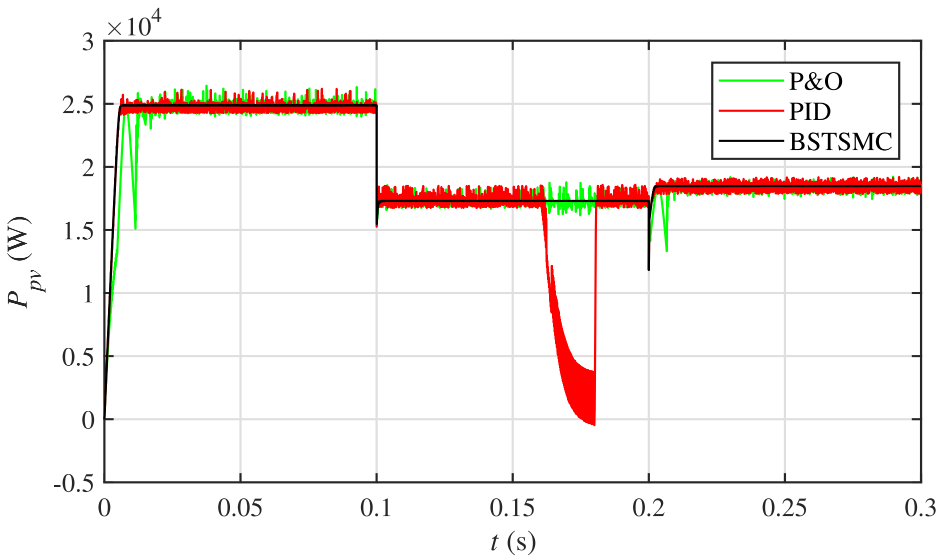

Figure 22. PV array output power comparison in Case 5.

8. Conclusions

To optimize the electric power extraction from a standalone PV array under inconsistent ambient weather conditions that is delivering power to a resistive load through a CCNI-BuBo converter, in this article, a hybrid nonlinear sensorless observer based robust BSTSMC MPPT strategy is proposed. The reference peak power voltage is generated via the GPR based probabilistic machine learning approach that is adequately tracked by the proposed MPPT scheme. All the missing system states are retrieved through the GSTA based DFA approach. The Lyapunov stability theory is used to guarantee the closed-loop system stability. Matlab/Simulink software platform is used for simulation, testing and performance validation of the proposed MPPT strategy under simultaneous variation of the temperature, irradiance and load. When the MPPT performance of the proposed MPPT scheme is compared with the recently proposed benchmark backstepping based MPPT control strategy [13] and other conventional SMC, PID and P&O based MPPT schemes, the proposed technique is found to have a superior performance in terms of offering a fast dynamic response, finite-time convergence, minute chattering, higher tracking accuracy and having more robustness against plant parameter perturbations, load disturbances and certain time-varying sinusoidal faults occurring in the system.

Author Contributions: R.K. developed the concept, conducted simulations and wrote the initial draft; L.K. and J.-S.R. supervised this research work; S.U. and I.S. analyzed the data and reviewed the manuscript. All authors have read and agreed to the published version of the manuscript.

Funding: This research was supported by Basic Science Research Program through the National Research Foundation of Korea funded by the Ministry of Education (2016R1D1A1B01008058) and by Human Resources Development (No.20204030200090) of Korean Institute of Energy Technology Evaluation and Planning (KETEP) grant funded by the Korea government Ministry of Trade, Industry, and Energy.

Conflicts of Interest: The authors declare no conflict of interest.

Abbreviations

The following abbreviations have been used in this manuscript:

ANFIS	Adaptive NeuroFuzzy Inference System
BSTSMC	Backstepping Super-Twisting Sliding Mode Control
CCM	Continuous Conduction Mode
CCNI-BuBo	Cascaded Non-inverting Buck-Boost
CSMC	Conventional Sliding Mode Control
DFA	Differential Flatness Approach
GP	Gaussian Process
GPR	Gaussian Process Regression
GSTA	Generalized Super-Twisting Algorithm
MPP	Maximum Power Point
MPPT	Maximum Power Point Tracking
P&O	Perturb and Observe
PID	Proportional Integral Derivative Control
PV	Photovoltaic
RMSE	Root Mean Square Error
SEPIC	Single-Ended Primary Inductor
SMC	Sliding Mode Control
STA	Super-Twisting Algorithm
STC	Standard Test Condition
VSC	Variable-Structure Control

Nomenclature

A	Diode ideality factor (or constant)
C_1	Input capacitor (F)
C_2	Output capacitor (F)
d	Duty cycle
D_1, D_2	Diodes
$\mathcal{GP}$	Gaussian process
I	PV cell output current (A)
I_0	Diode leakage (or reverse saturation) current (A)
I_D	Diode current (A)
i_L	Inductor current (A)
I_p	Current through the shunt resistance (A)
I_{ph}	Photon-generated current (A)
i_{pv}	PV array output current (A)
k	Boltzmann constant (1.38×10^{-23} J/K)
$\mathcal{K}_{\mathcal{SE}}$	Squared exponential covariance or kernel function
L	Inductance (H)
ℓ	Characteristic length-scale

N_p	Number of parallel connected PV modules
N_s	Number of series connected PV cells
P_{MPP}	Power at maximum power point (W)
q	Electron charge (1.6×10^{-19} C)
r	Radial basis function
R_s	Series resistance (Ω)
R_p	Shunt resistance (Ω)
T	Temperature (°C)
u	Control input
V	PV cell output voltage (V)
$v_{C_2} = v_{R_L}$	Load voltage (V)
V_{f1}, V_{f2}	Lyapunov function candidates
V_{MPP}	Voltage at maximum power point (V)
$v_{pv} = v_{C_1}$	PV array output voltage (V)
v_{pv}^r	PV array reference (or desired) output voltage (V)
β	Inductor current reference (A)
c_1, c_2	Constants
ϵ_1	PV array output voltage error (V)
ϵ_2	Inductor current error (A)
$\kappa_1, \kappa_2, \kappa_3, \kappa_4$	Constants
λ	Constant
μ	Mean
ζ	Observation error

Appendix A. Convergence Analysis of the GSTA Based Differentiators

This appendix, covers the convergence analysis of the three GSTA based differentiators depicted in Figure 5. This analysis is carried out by applying two standard test input signals, i.e., a unit step signal and a sawtooth signal to the differentiators. All the three differentiators are tuned manually and their tuning parameters are specified in Table A1. As illustrated in Figures A1 and A2, all the three differentiators accurately estimate both the input signals with almost zero root mean square error (RMSE), thus guaranteeing the convergence. Moreover, the stability of the differentiator is guaranteed, if:

$$\lim_{t\to\infty} \begin{pmatrix} \begin{pmatrix} x_i \\ x_{i+1} \end{pmatrix}_{Step} \\ \begin{pmatrix} x_i \\ x_{i+1} \end{pmatrix}_{sawtooth} \end{pmatrix} = \begin{pmatrix} \begin{pmatrix} \widehat{x}_i \\ \widehat{x}_{i+1} \end{pmatrix}_{Step} \\ \begin{pmatrix} \widehat{x}_i \\ \widehat{x}_{i+1} \end{pmatrix}_{sawtooth} \end{pmatrix} \tag{A1}$$

Table A1. Tuning parameters of the differentiators (from left to right in Figure 5).

Name	Constant	Value
Differentiator-1	Constant, c_1	200
	Constant, c_2	120
	Constant, λ	50
Differentiator-2	Constant, c_1	150
	Constant, c_2	900
	Constant, λ	8
Differentiator-3	Constant, c_1	15
	Constant, c_2	35
	Constant, λ	170

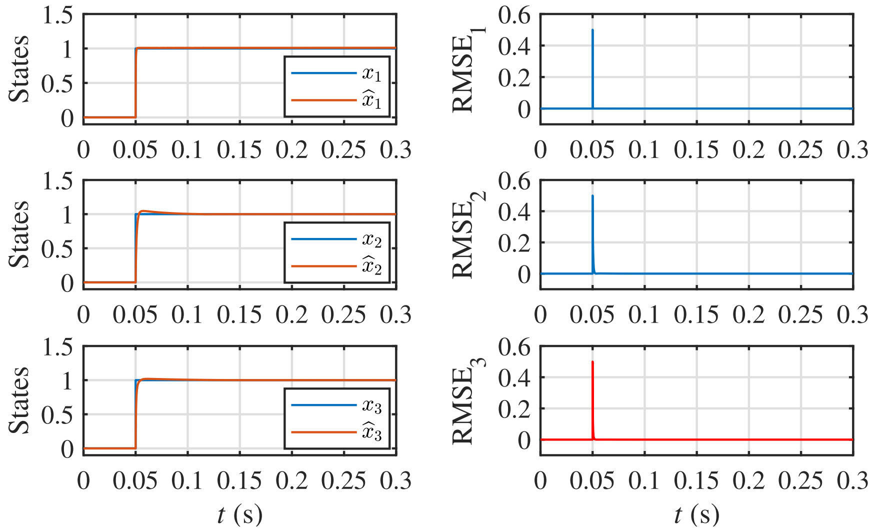

Figure A1. Convergence analysis of the differentiator for a step input signal and the corresponding RMSE.

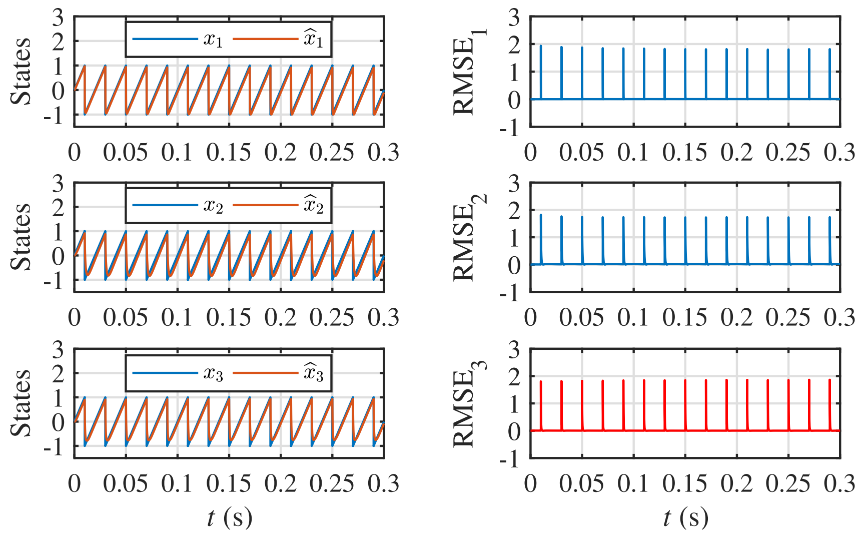

Figure A2. Convergence analysis of the differentiator for a sawtooth input signal and the corresponding RMSE.

Appendix B. Zero Dynamics State Stability Analysis

In this appendix, the stability analysis of the zero dynamics state, x_3, is briefly described. As, Equation (35) represents a three-step BSTSMC based MPPT law, hence, the following expression gives the internal dynamics of the system:

$$\dot{x}_3 = \frac{(1-u)x_2}{C_2} - \frac{x_3}{R_L C_2} \tag{A2}$$

The zero dynamics state, x_3, can be deduced by substituting both the control driven states (x_1, x_2) and the applied control input (u) equal to zero into Equation (A2), thus it yields:

$$\dot{x}_3 = -\frac{x_3}{R_L C_2} \tag{A3}$$

As, both the parameters C_2 and R_L are positive constants, thus, Equation (A3) has roots/zeros in the left-half of the *s*-plane, located at $-\frac{1}{R_L C_2}$. It means that zero dynamics are exponentially stable and the system under consideration is a minimum phase system. The convergence analysis of the zero dynamics state, x_3, is illustrated in Figure A3, while the corresponding zeros location is depicted in Figure A4 on the s-plane, where $R_L C_2 = \tau$ represents the *RC*-time constant.

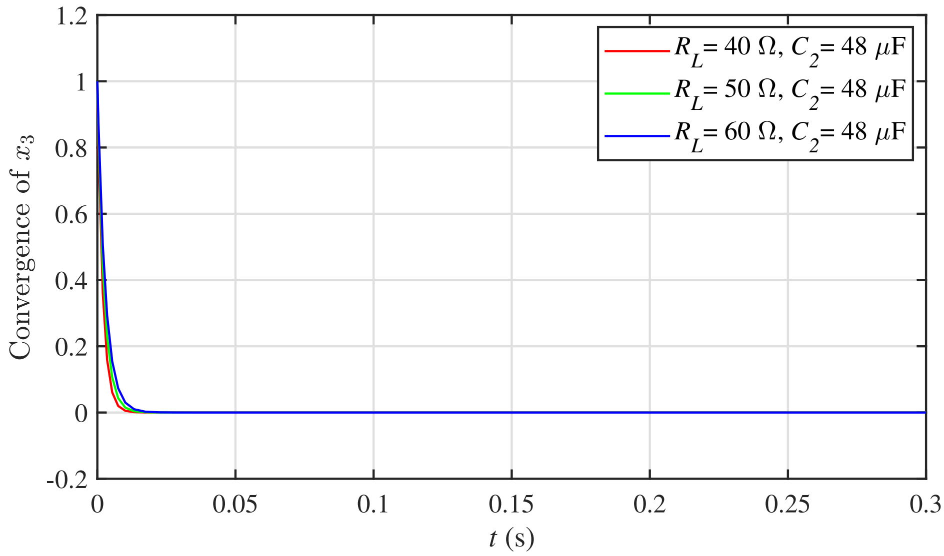

Figure A3. Zero dynamics state, x_3, convergence analysis.

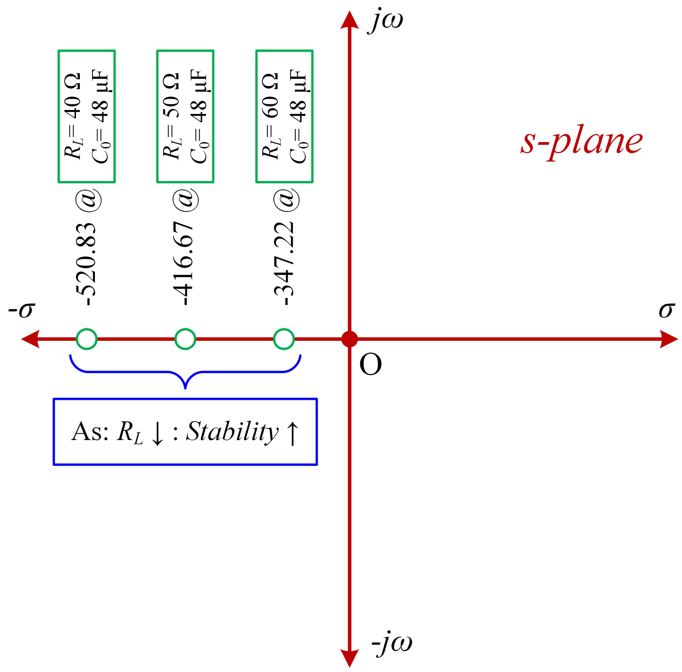

Figure A4. Complex-plane for the internal dynamics.

References

1. Dahech, K.; Allouche, M.; Damak, T.; Tadeo, F. Backstepping sliding mode control for maximum power point tracking of a photovoltaic system. *Electr. Power Syst. Res.* **2017**, *143*, 182–187. [CrossRef]
2. De Brito, M.A.G.; Galotto, L.; Sampaio, L.P.; e Melo, G.D.A.; Canesin, C.A. Evaluation of the main MPPT techniques for photovoltaic applications. *IEEE Trans. Ind. Electron.* **2012**, *60*, 1156–1167. [CrossRef]

3. Chaibi, Y.; Salhi, M.; El-Jouni, A. Sliding mode controllers for standalone PV systems: Modeling and approach of control. *Int. J. Photoenergy* **2019**, 1–12. [CrossRef]
4. Youssef, A.; El Telbany, M.; Zekry, A. Reconfigurable generic FPGA implementation of fuzzy logic controller for MPPT of PV systems. *Renew. Sustain. Energy Rev.* **2018**, *82*, 1313–1319. [CrossRef]
5. Yilmaz, U.; Kircay, A.; Borekci, S. PV system fuzzy logic MPPT method and PI control as a charge controller. *Renew. Sustain. Energy Rev.* **2018**, *81*, 994–1001. [CrossRef]
6. Al-Dhaifallah, M.; Nassef, A.M.; Rezk, H.; Nisar, K.S. Optimal parameter design of fractional order control based INC-MPPT for PV system. *Sol. Energy* **2018**, *159*, 650–664. [CrossRef]
7. Tey, K.S.; Mekhilef, S.; Seyedmahmoudian, M.; Horan, B.; Oo, A.T.; Stojcevski, A. Improved differential evolution-based MPPT algorithm using SEPIC for PV systems under partial shading conditions and load variation. *IEEE Trans. Ind. Inf.* **2018**, *1*, 4322–4333. [CrossRef]
8. Gil-Antonio, L.; Saldivar, B.; Portillo-Rodríguez, O.; Ávila-Vilchis, J.C.; Martínez-Rodríguez, P.R.; Martínez-Méndez, R. Flatness-based control for the maximum power point tracking in a photovoltaic system. *Energies* **2019**, *12*, 1843. [CrossRef]
9. Chowdhury, D.; Hasan, A.K.; Khan, M.Z. Islanded DC Microgrid Architecture with Dual Active Bridge Converter-Based Power Management Units and Time Slot-Based Control Interface. *IEEJ Trans. Electr. Electron. Eng.* **2020**, *15*, 863–871. [CrossRef]
10. Hasan, A.S.; Chowdhury, D.; Khan, M.Z. Scalable DC microgrid architecture with a one-way communication based control Interface. In Proceedings of the 2018 10th International Conference on Electrical and Computer Engineering (ICECE), Dhaka, Bangladesh, 20–22 December 2018; pp. 265–268.
11. Chowdhury, D.; Hasan, A.S.; Khan, M.Z. Scalable DC microgrid architecture with phase shifted full bridge converter based power management unit. In Proceedings of the 2018 10th International Conference on Electrical and Computer Engineering (ICECE), Dhaka, Bangladesh, 20–22 December 2018; pp. 22–25.
12. Arsalan, M.; Iftikhar, R.; Ahmad, I.; Hasan, A.; Sabahat, K.; Javeria, A. MPPT for photovoltaic system using nonlinear backstepping controller with integral action. *Sol. Energy* **2018**, *170*, 191–200. [CrossRef]
13. Naghmash; Armghan, H.; Ahmad, I.; Armghan, A.; Khan, S.; Arsalan, M. Backstepping based non-linear control for maximum power point tracking in photovoltaic system. *Sol. Energy* **2018**, *159*, 134–141. [CrossRef]
14. Ali, K.; Khan, L.; Khan, Q.; Ullah, S.; Ahmad, S.; Mumtaz, S.; Karam, F.W.; Naghmash. Robust Integral Backstepping Based Nonlinear MPPT Control for a PV System. *Energies* **2019**, *12*, 3180. [CrossRef]
15. Krstić, M.; Kokotović, P.V.; Kanellakopoulos, I. *Nonlinear and Adaptive Control Design*; John Wiley & Sons, Inc.: New York, NY, USA, 1995.
16. Krstić, M.; Smyshlyaev, A. *Boundary Control of PDEs: A Course on Backstepping Designs*; Society for Industrial and Applied Mathematics (SIAM): Phildelphia, PA, USA, 2008.
17. Zhang, F.; Maddy, J.; Premier, G.; Guwy, A. Novel current sensing photovoltaic maximum power point tracking based on sliding mode control strategy. *Sol. Energy* **2015**, *118*, 80–86. [CrossRef]
18. Li, S.; Yu, X.; Fridman, L.; Man, Z; Wang, X. *Advances in Variable Structure Systems and Sliding Mode Control—Theory and Applications*; Springer International Publishing: Cham, Switzerland, 2017.
19. Castillo, I.; Fridman, L.; Moreno, J.A. Super-twisting algorithm in presence of time and state dependent perturbations. *Int. J. Control* **2018**, *91*, 2535–2548. [CrossRef]
20. Mohd Zaihidee, F.; Mekhilef, S.; Mubin, M. Robust speed control of PMSM using sliding mode control (SMC)—A review. *Energies* **2019**, *12*, 1669. [CrossRef]
21. Kchaou, A.; Naamane, A.; Koubaa, Y.; M'sirdi, N. Second order sliding mode-based MPPT control for photovoltaic applications. *Sol. Energy* **2017**, *155*, 758–769. [CrossRef]
22. Chalanga, A.; Kamal, S.; Fridman, L.M.; Bandyopadhyay, B.; Moreno, J.A. Implementation of super-twisting control: Super-twisting and higher order sliding-mode observer-based approaches. *IEEE Trans. Ind. Electron.* **2016**, *63*, 3677–3685. [CrossRef]
23. Shtessel, Y.; Edwards, C.; Fridman, L.; Levant, A. *Sliding Mode Control and Observation*; Springer Science+ Bussiness Media: New York, NY, USA, 2014.
24. Villalva, M.G.; Gazoli, J.R.; Ruppert Filho, E. Comprehensive approach to modeling and simulation of photovoltaic arrays. *IEEE Trans. Power Electron.* **2009**, *24*, 1198–1208. [CrossRef]
25. Kim, I.S. Robust maximum power point tracker using sliding mode controller for the three-phase grid-connected photovoltaic system. *Sol. Energy* **2007**, *81*, 405–414. [CrossRef]

26. Kanwal, S.; Khan, B.; Ali, S.M.; Mehmood, C.A. Gaussian process regression based inertia emulation and reserve estimation for grid interfaced photovoltaic system. *Renew. Energy* **2018**, *126*, 865–875. [CrossRef]
27. Rasmussen, C.E.; Williams, C.K.I. *Gaussian Processes for Machine Learning*; The MIT Press: Cambridge, MA, USA, 2006.
28. Almasi, O.N.; Fereshtehpoor, V.; Khooban, M.H.; Blaabjerg, F. Analysis, control and design of a non-inverting buck-boost converter: A bump-less two-level T–S fuzzy PI control. *ISA Trans.* **2017**, *67*, 515–527. [CrossRef] [PubMed]
29. Ang, S.; Oliva, A.; Griffiths, G.; Harrison, R. *Power-Switching Converters*; CRC Press, Taylor & Francis Group: Boca Raton, FL, USA, 2010.
30. Olaru, S.; Grancharova, A.; Pereira, F.L. *Developments in Model-Based Optimization and Control*; Springer International Publishing: Cham, Switzerland, 2015.
31. Levant, A. Robust exact differentiation via sliding mode technique. *Automatica* **1998**, *34*, 379–384. [CrossRef]
32. Cruz-Zavala, E.; Moreno, J.A.; Fridman, L.M. Uniform robust exact differentiator. *IEEE Trans. Autom. Control* **2011**, *56*, 2727–2733. [CrossRef]
33. Fliess, M.; Lévine, J.; Martin, P.; Rouchon, P. Flatness and defect of non-linear systems: Introductory theory and examples. *Int. J. Control* **1995**, *61*, 1327–1361. [CrossRef]
34. Slotine, J.J.E.; Li, W. *Applied Nonlinear Control*; Prentice Hall Englewood Cliffs: Englewood Cliffs, NJ, USA, 1991.
35. Marquez, H.J. *Nonlinear Control Systems: Analysis and Design*; John Wiley & Sons: Hoboken, NJ, USA, 2003.